Journal of the Meteorological Society of Japan

EARLY ONLINE RELEASE

The DOI for this manuscript is
DOI:10.2151/jmsj.2022-014
J-STAGE Advance published date: November 12th, 2021
The final manuscript after publication will replace the preliminary version at the above DOI once it is available.

Influence of the Madden-Julian Oscillation on Wintertime Extreme Snowfall and Precipitation in Japan

Chiharu TAKAHASHI[1*], Yukiko IMADA[2],

and Masahiro WATANABE[1]

[1] *Atmosphere and Ocean Research Institute, the University of Tokyo, Chiba, Japan*

[2] *Meteorological Research Institute, Japan Meteorological Agency, Tsukuba, Japan*

1[*]) Corresponding author: Chiharu Takahashi

5-1-5, Kashiwanoha, Kashiwa, Chiba, 277-8568, JAPAN

Email: chiha@aori.u-tokyo.ac.jp

Tel: +81-4-7136-4393

Abstract

The present study found a significant influence of the Madden-Julian Oscillation (MJO) on the occurrence probability of extreme snowfall and precipitation in Japan during boreal winter (December-February) using observational data and the Database for Policy Decision Making for Future Climate Change (d4PDF). The analysis of d4PDF containing 90-member and 50-member ensemble historical simulations by global and high-resolution regional models, respectively, enabled us to quantify and elucidate the geographical distribution of the occurrence probability of extreme weather in Japan related to the MJO. The d4PDF global simulations well represent the MJO and its teleconnection over the Pacific-North America region.

Our results show that (1) the probability of extreme snowfall on the Sea of Japan side of northwestern Japan (SJA) increases (decreases) by approximately 20% (30-40%) associated with enhanced MJO over the Maritime Continent and western Pacific (western Indian Ocean) relative to that for all winter days; (2) the extreme precipitation on the Pacific Ocean side (PAC) of Japan increases (reduces) by 40-50% (approximately 30%) when the MJO is active over the Indian Ocean (western Pacific); and (3) the extreme snowfall on the Kanto area in PAC increases by 30-45% when the MJO is enhanced over the eastern Indian Ocean and Maritime Continent. Composite analysis reveals that different physical processes associated with the MJO are responsible for the occurrence of extremes in the three regions. The MJO intensifies cold air intrusion from Siberia into Japan associated with a more frequent blocking over East

Siberia, causing extreme snowfall in SJA. The MJO stimulates the explosive development of extratropical cyclones due to enhanced moisture flux convergence, leading to extreme precipitation in PAC and extreme snowfall in Kanto. Furthermore, the Kanto snowfall is partly related to a cold air outflow from the blocking induced by the MJO.

Keywords MJO teleconnection, extreme snowfall and precipitation, AGCM, regional climate model, large ensemble simulation

1 Introduction

Severe snowfall and precipitation events over the Sea of Japan side and Pacific Ocean side of the islands of Japan (Fig. 1) are empirically known to be associated with different synoptic weather patterns. On the Sea of Japan side, precipitation is largely dominated by snowfall, and it is statistically known that normal snowfall is caused by intensified northwesterly monsoon flow (winter monsoon pattern), which is dry and cold air originating from Siberia with the development of the Siberian high and Aleutian low and becomes unstable by heat and moisture supply over the Sea of Japan. Previous studies have investigated the mechanism of heavy snowfall on the Sea of Japan side in terms of synoptic-to-large scale atmospheric circulations (e.g., Yamashita et al. 2012; Ueda et al. 2015; Kawase et al. 2018). Extreme snowfall occurrences on the Sea of Japan side link to intermittent cold air outbreaks (CAO; e.g., Iwasaki et al, 2014; Shoji et al. 2014), referred to as cold surge intrusions into East Asia via Siberia

(Yamashita et al. 2012; Sasai et al. 2019), and are related to intraseasonal atmospheric blocking in the East Siberian region (Yamazaki et al. 2019). The interannual variability of the occurrence of heavy snowfall is related to an anomalous cyclonic circulation over Japan formed as the stationary Rossby wave response to intensified tropical convection over maritime continents and neighboring oceans (Ueda et al. 2015), and extraordinary intensification of the East Asian winter monsoon circulation associated with combined forcing of El Niño-Southern Oscillation (ENSO) and North Atlantic Oscillation (NAO) (Sakai and Kawamura, 2009).

On the Pacific Ocean side of southern Japan, including Kanto, precipitation is mostly dominated by rainfall, and there is less snowfall compared to the Sea of Japan side. Although few studies have focused on snowfall events on Japan's Pacific Ocean side, the Kanto area infrequently experiences extraordinarily heavy snowfall. This occurrence is mostly caused by the development of an extratropical cyclone passing along the southern coast of Japan (south coastal cyclone pattern) (Honda et al. 2016; Kawase et al. 2018) and is to some extent regulated by northwestern Pacific blocking, leading to a strong cold-air inflow (Yamazaki et al. 2015). However, it is incompletely understood what intraseasonal variabilities and how they control synoptic situations for heavy snowfalls and extreme rainfall in Japan, although a previous study mentioned the relation of Eurasian patterns (Wallace and Gutzlar 1981) to interannual variations in snowfall events at one observational site in southern Japan (Tachibana et al. 2007).

The Madden-Julian Oscillation (MJO) is the most dominant mode of tropical intraseasonal variability (Madden and Julian 1972), which manifests as an eastward propagating mode of convection and atmospheric circulation and has the largest amplitude during boreal winter (e.g., Zhang 2005; Jiang et al. 2020). MJO-related convective heating excites a poleward dispersion of the Rossby wave train and generates a local Hadley circulation, which can modulate extratropical atmospheric circulation (MJO-teleconnection) and thus globally affect mid- to high-latitude weather changes (e.g., Matthews et al. 2004; Zhang et al. 2013; Seo and Lee 2016; Stan et al. 2017). The MJO-teleconnections are a key source of global weather predictability on the extended subseasonal timescale of about 10-40 day (Robertson et al, 2015). In East Asia, MJO-related convection influences subseasonal variability in precipitation and surface temperature (Jeong et al. 2008; He et al. 2011) and high-impact weather during the winter, the occurrences of the cold surge and CAO (Jeong et al. 2005; Abdillah et al. 2018) and heavy snowfall events over Korea (Park et al. 2010).

The MJO affects the variations in North Pacific storm track activity (Deng and Jiang 2011; Takahashi and Shirooka 2014) and extratropical cyclones (Guo et al. 2017) due to interactions between synoptic eddies and MJO-induced flow anomalies. The enhanced activity of these extratropical storms can cause severe weather in midlatitude populated areas. Some previous studies have shown that MJO teleconnection is linked to significant changes in Northern Hemisphere winter blocking (Moore et al. 2010, Henderson et al. 2016). Henderson et al. (2016) demonstrated that a significant increase (decrease) in blocking frequency over the west and central Pacific occurs when MJO-related convection is enhanced in the western Pacific (Indian Ocean). Extreme cold events over Korea are partly associated with Subarctic (East

Siberian) blocking (Park et al. 2019). Hence, it is expected that the wintertime blocking associated with the MJO impacts extreme cold events and heavy snowfall in East Asia, including northern China, Korea, and Japan.

Recently, some studies have presented the quantitative impacts of the MJO on the occurrence frequency of extreme wintertime rainfall in southeast Asia (Xavier et al. 2014) and southern China (Ren and Ren 2017). Ren and Ren (2017) indicated that the probability of extreme rainfall events in southern China increased (decreased) by 30-50% (20-40%) relative to all days in the winter when the enhanced MJO convection was enhanced over the Indian Ocean (western Pacific). Matsueda and Takaya (2015) demonstrated that the frequency of winter extreme temperature events is significantly modulated by the MJO over some areas in the extratropics such as Asia, America, and Europe.

Although the understanding of the impact of the MJO on rainfall and temperature variations has progressed, the influence of the MJO on the geographical distribution and occurrence frequency of extreme snowfall and rainfall in Japan remains unclear. Due to the severe impacts of heavy snowfall, understanding the mechanisms driving the occurrence and the source of predictability are critical issues to improve projections' uncertainty. Observed extreme events for each MJO phase occur not too frequently to significantly and quantitatively estimate occurrence probability. In addition, a low-resolution global climate model (GCM) cannot represent the geographical distribution of extreme events in Japan. Therefore, we use a large ensemble dataset, "Database for Policy Decision Making for Future Climate Change (d4PDF)"

(Mizuta et al. 2017) containing high-resolution regional and global model (MRI-AGCM3.2) simulations with the horizontal resolutions of 20 km and 60 km, respectively. As this global model has relatively good skill of the MJO compared to other current GCMs (Wang et al. 2020b), the analysis of d4PDF with a large-ensemble simulation of the regional model enable us to quantitatively estimate and elucidate the geographical distribution of the occurrence probability of extreme weather in Japan associated with MJO, which has not been clarified. We investigate the influence of the MJO on extreme snowfall and precipitation on the Sea of Japan side and Pacific Ocean side of Japan.

The remaining parts of the paper are organized as follows. The dataset and methodology are described in Section 2. The simulation skills to represent MJO and MJO teleconnection in the d4PDF dataset are evaluated in Section 3. Section 4 presents the influence of the MJO on extreme wintertime snowfall and precipitation in Japan. Sections 5 and 6 describe the characteristics of atmospheric circulation patterns and the underlying mechanisms to link the occurrence of extreme events with the MJO, respectively. Conclusions and discussions are provided in section 7.

2 Data and Methods

2.1 Data

We used a large number of ensemble simulation data from the d4PDF, which consists of outputs from a global atmospheric model (MRI-AGCM3.2) with a horizontal grid spacing of

60 km and from regional downscaling simulations covering the Japan area by a nonhydrostatic regional climate model (NHRCM) with a 20-km grid spacing (Fig. 1a). In this study, 90-member and 50-member ensemble historical simulations from the output for GCM and RCM, respectively, were used for the analysis period during boreal winter (December-February, DJF) in 1979-2018.

We also used daily gridded precipitation and temperature datasets with a spatial resolution of 0.25° provided by the Asian Precipitation-Highly Resolved Observational Data Integration Towards the Evaluation of Water Resources (APHRODITE) project (Yatagai et al. 2012). Daily snowfall data in Japan were obtained from observational station data of the Automated Meteorological Data Acquisition System (AMeDAS) operated by the Japan Meteorological Agency. The data of available stations are spatially interpolated with a 0.25° horizontal grid. Atmospheric variables were derived from the Japanese 55-Year Reanalysis (JRA55) Project (Kobayashi et al., 2015) dataset with a 1.25° horizontal and 6-hourly resolutions. The daily outgoing longwave radiation (OLR) and daily precipitation data interpolated from the pentad data with a 2.5° spatial resolution from the Global Precipitation Climatology Project (GPCP), (Adler et al., 2003) were utilized. Considering the reliability and availability of the observational data, we analyzed winter precipitation for 1979-2015 and the other data for 1979-2018. Daily anomalies were derived relative to 1981-2010 climatology. We applied a 5-day running mean filter to the daily data in order to smooth small-scale noise.

2.2 Methods

The phases and amplitude of the MJO are derived from the daily multivariate MJO (RMM) index (Wheeler and Hendon 2004). The MJO indices are the first two principal components of the combined empirical orthogonal functions (CEOFs) of 15°S-15°N averaged OLR and 850- and 200-hPa zonal winds anomalies. The observed MJO indices are calculated from the winds data of JRA55. Although some previous studies for the model comparison of the MJO use the observation-based CEOFs for consistent comparison among the models (Henderson et al. 2017) or model-based CEOFs (Ahn et al. 2017). The former projection method possibly produce artificially higher MJO simulation skills in the models (Ahn et al. 2017). Our study first evaluates the MJO and MJO-teleconnection characteristics in d4PDF. Therefore, the MJO indices for d4PDF are obtained by projecting OLR and zonal wind anomalies for each member onto the CEOF of one reference member, which is randomly picked because we confirmed that the first two CEOFs modes have almost the same patterns among all ensemble members. The anomalies are derived by subtracting the previous 120-day mean to reduce the influence of interannual variability and the first three harmonics of the climatological seasonal cycle. MJO-phase composites are constructed for days with normalized amplitudes of MJO indices greater than one standard deviation (std). Although the lag-composite is often applied in the regions such as North America and Europe where the propagation of Rossby wave in each MJO phase is delayed, we show the composites in MJO phases at lag 0 (day 0) after section 4 since Japan is closer to active region of MJO. We apply 10-80-day and 20-80-day bandpass-filter as intraseasonal time scales appropriately to show tropical MJO signal and MJO-extratropical response, respectively.

Extreme precipitation (snowfall) days were defined as days exceeding the 95th percentile value of daily precipitation (snowfall) amounts above 0.1 mm day^{-1} (0.1 cm day^{-1}) on all days in DJF based on the percentile-based threshold method (Zhang et al. 2011). An extreme cold day was also defined as a day falling below the 5th percentile of temperature during all winter days. As another threshold of extreme events, the 90th or 10th percentile values were also used.

The percentage change in the extreme events for the MJO phases is calculated as follows (Ren and Ren 2017):

$$\Delta P_{MJO} = \frac{P_{MJO}\,(x \geqq x_c) - P_{all}\,(x \geqq x_c)}{P_{all}\,(x \geqq x_c)} * 100\ \% \qquad (1)$$

Here, ΔP_{MJO} is the percentage change in the cumulative probability of precipitation or snowfall (x) exceeding a percentile threshold (x_c) due to the MJO. $P_{MJO}(x \geqq x_c)$ is the cumulative probability exceeding x_c calculated for only the days in a given MJO phase (MJO amplitude $\geqq$ 1.0 std), and $P_{all}(x \geqq x_c)$ is calculated for all days during the winter season. In the same way, the percentage change in the extreme cold events falling below x_c was calculated from $P_{MJO}(x \leqq x_c)$ and $P_{all}(x \leqq x_c)$.

To detect atmospheric blocking, the Northern Hemisphere blocking index developed by Tibaldi and Molteni (1990) is used in this study. The gradient of the geopotential height at 500 hPa smoothed by a 5-day running mean is calculated in the southern and northern parts for each longitude. A given longitude is regarded as blocked if the meridional gradients fulfill the threshold on a given day. The definition is described in more detail in Tibaldi and Molteni (1990).

3. MJO and MJO teleconnection simulated in d4PDF

Previous multimodel comparison studies have demonstrated that a global climate model, MRI-CGCM3 (Yukimoto et al. 2012), and the atmospheric component, MRI-AGCM3, which is the same as a model used by d4PDF, reasonably simulate the observed MJO signal (Rushley et al. 2019, Wang et al. 2020b). However, they analyzed only one member of each model. Here, we confirm the representation of the MJO during the winter by a large ensemble simulation in d4PDF. The observed lag-regression diagram of equatorial 20-80 day filtered precipitation anomaly against the Indian Ocean base point shows continuous eastward propagation from the Indian Ocean to the western Pacific at a phase speed of approximately 6 ms^{-1} with the low-level zonal wind anomaly lagging 5-10 days behind (Fig. 2a). The ensemble means of each lag-regression in d4PDF capture the eastward propagation of precipitation and zonal wind well (Fig. 2b), which exhibits high skill with pattern correlation exceeding 0.8 of lag-regressed precipitation anomalies on a time-longitude domain of 60°-180°E and day -20 to day 20 between the simulated and observed patterns.

The wavenumber-frequency spectral variance normalized by background spectra following Wheeler and Kiladis (1999) is displayed for the symmetric component of equatorial precipitation in GPCP and d4PDF (Figs. 2c, d). The observed spectrum shows a distinct variance peak corresponding to the MJO with wavenumbers 1-5 and frequencies from 1/90 to 1/20 cycle per day (Fig. 2c). Equatorial Kelvin and Rossby waves have large variances in the equivalent depth range of 12-50 m. The d4PDF exhibits a strong variance maximum in the MJO spectral band that is clearly separated from that of the Kelvin wave, as in the observation (Fig. 2d). Although one reference member is shown here, we confirmed that other members have similar spectrums to this (not shown).

The MJO-extratropical teleconnection pattern in d4PDF is examined and compared to that in the observation. Figure 3 shows the composite of intraseasonal circulation and convective anomalies in MJO phases 1-8 for the observation and d4PDF. The observed teleconnection patterns in the midlatitude northwestern Pacific indicate anticyclonic and cyclonic circulation anomalies, along with OLR negative and positive anomalies over Japan in MJO phases 2-4 and 6-8, respectively (Fig. 3a). In the d4PDF, the phase changes in the circulation response over the northwestern Pacific and anomalous convection around Japan are qualitatively in good agreement with those of the observations (Fig. 3b).

To quantitatively compare the simulation capability of d4PDF to those of CMIP5 models, we calculate skill metrics of the MJO (MS1-MS2) and MJO teleconnection (TS1-TS4) defined by Wang et al. (2020a, b) for all MJO phases in d4PDF (Figs. 4 and S1). For the skill metric of the MJO teleconnection pattern (TS1), the pattern correlation coefficient (pattern CC) of 500-hPa geopotential height (Z500) anomaly composites is calculated between JRA55 and d4PDF over the Pacific-North America (PNA) region (20°N-80°N, 120°E-60°W; yellow box in Fig.

3a) averaged over 5-9 days after each MJO phase. TS1 of the ensemble mean anomalies (red numbers) are larger than the ensemble mean of TS1 (purple circles) for each phase (Fig. 4a) and show higher values in phase 2 (0.81), phase 3 (0.72), and phase 7 (0.7) compared with those for phase 2 (0.61), phase 3 (0.65), and phase 7 (0.64) in the multimodel mean of CMIP5 (Wang et al. 2020a). This result means that the large-ensemble mean can yield a better signal of the teleconnection pattern because of the noise reduction. The pattern CCs of 500-hPa stream function (ψ500) anomalies show higher values than those of Z500 for each phase (Fig. S1a).

For the skill metric of the MJO pattern (MS1), pattern CC between d4PDF and observed OLR anomaly composites is calculated over the tropical Indo-Pacific region (40°E-140°W, 15°S-15°N) averaged over 0-4-day lag. The MS1 of the ensemble mean anomalies (red numbers) for phase 3 (0.76), phase 7 (0.77), and all phases (0.8) are larger than those in the multimodel mean of CMIP5 (Wang et al. 2020b).

The Rossby wave source (RWS; Sardeshmukh and Hoskins 1988) is often examined to diagnose the origin of Rossby wave propagation. The RWS consists of a component of vorticity generation by a divergence of the upper-level divergent winds and a component of absolute vorticity advection by divergent winds. For the process-based metric, pattern CCs of RWS (TS3) are calculated from composites of 250-hPa RWS anomalies over the region (10°-45°N, 60°E-120°W; yellow box in Fig. S1f) (Figs. S1f-i) on 0-4-day lag in a similar way as TS1. The d4PDF can reasonably reproduce the pattern of RWS with a pattern CC equal to 0.7 for MJO at all phase means (Fig. 4b). The correlation coefficients (r) between MS1 and TS3, TS3 and

TS1, and MS1 and TS1 are significant positive values with 0.57, 0.55, and 0.46, respectively (gray numbers) when they are estimated from all members for all MJO phases and have significantly higher values with 0.73, 0.86, and 0.95, respectively (purple numbers) when they are estimated from the ensemble mean of metrics for each phase (purple circles) (Figs. 4a, b, and S1a, b). The above results indicate that a more realistic MJO pattern produces more reasonable teleconnection patterns via a more consistent RWS pattern.

For skill metrics representing the magnitude of simulated anomalies, the relative amplitudes of the MJO (MS2), MJO teleconnection over the PNA region (TS2), and RWS (TS4) in d4PDF to those of the observations are similarly calculated from the standard deviations of anomaly composites over the regions same as MS1, TS1, and TS3, respectively. The ensemble means of MS2 on 0-4-day lag and TS2 on 5-9-day lag for phase 3 (phase 7) are 0.86 (0.83) and 1.1 (1.2), respectively (Figs. 4c, d), which is consistent with the feature that most CMIP5 models tend to underestimate MS2 and overestimate TS2 for phases 3 and 7 (Wang et al. 2020a, b). The relationships between MS2 and TS4 and TS4 and TS2 show significant high correlations for all MJO phases (Figs. 4d, and S1c), whereas the correlation between MS2 and TS2 has a lower value (Fig. 4c). This result suggests that more enhanced MJO convection not necessarily produces stronger MJO teleconnection, because the nonlinear wave-mean flow interaction also may lead to the variation in amplitude of MJO teleconnection (Wang et al. 2020a). We also show several metrics derived from MJO indices using the observation-based CEOF, which is marked with an asterisk (Figs. S1d, e). The ensemble means of MS1*, TS1*, and MS2* show somewhat higher values than those using the CEOF based on one-member in d4PDF, respectively (Figs. 4a, c and S1d, e).

Additionally, we examined three other skill metrics of the MJO teleconnection: east-west position (TS5), intraphase pattern consistency (IPC, TS6), and persistence (TS7) following Wang et al. (2020a) (see Fig. S2 for details). The result of TS5 indicates that the MJO teleconnection in d4PDF tends to exhibit eastward shifted patterns for all phases compared to the observation, which is found in most CMIP5 models, as shown in Wang et al. (2020a) (Fig. S2a). This bias is likely due to an eastward and southward shifted subtropical jet (Figs. S1j, k). For TS6, the d4PDF ensemble mean shows a similar result of an interphase change to the observation (correlation of 0.94), with phases 2, 3, 7, and 8 having more consistent teleconnection patterns (Fig. S2b). For TS7, the observed teleconnection patterns for phases 3 and 7 have longer persistence than other phases, and d4PDF has a similar finding (Figs. S2c, d).

In short, the above results in comparison with CMIP5 models indicate that the ensemble means in d4PDF reproduce the MJO and its teleconnections well. As the simulation for d4PDF was performed using the observed monthly mean SST as the lower boundary condition, the above results suggest that a large ensemble simulation and SST pattern as well as a climatological subtropical jet play an important role in the reproduction of the MJO and thus its teleconnection patterns. Therefore, it is appropriate to investigate the influence of the MJO on extreme events over Japan using d4PDF.

4. Impacts of the MJO on extreme precipitation and snowfall in Japan

4.1 Variability of precipitation and snowfall in Japan during the winter

The winter mean and variance of precipitation and snowfall in Japan are shown in Figure 5. Dominant precipitation variation is found on the Pacific side and the Sea of Japan side (Fig. 5a). On the other hand, a large amount of snowfall and its significant variation appear on the Sea of Japan side, with relatively moderate snowfall on the Pacific Ocean side of northeastern Japan (Fig. 5b). The Kanto area (blue box in Fig. 1c) on the Pacific Ocean side infrequently experiences heavy snowfall, although it has a smaller amount of snowfall than the Sea of Japan side (Figs. 5b-d).

In this study, we focus on the three areas of the Sea of Japan side (SJA), the Pacific Ocean side (PAC), and the Kanto region (Kanto) and examine the extreme events of snowfall and precipitation. These regions are displayed in Fig. 1c. The snowfall amount in SJA has a high negative correlation with the surface temperature (correlation of -0.78) and exhibits a significant decreasing trend (Figs. 5c, f) in association with a warming trend in in Japan (Fig. 5g). However, snowfall in Kanto is less relevant to the temperature (correlation of -0.27) (Fig. 5f). Significant increasing trends are found in Kanto snowfall and PAC precipitation (Figs. 5d, e), which probably is linked to an increasing moisture trend (Fig. 5g). The results imply that snowfall variability in SJA is influenced by changes in the inflow of cold air masses, whereas snowfall in Kanto is not necessarily affected only by colder condition.

4.2. Influences of the MJO on extreme precipitation and snowfall

Figures 6 and 7 illustrate the distribution of the percentage change in the probability of extreme event occurrences over Japan for four MJO phases in which the MJO-related changes are more pronouncedly found in Japan. The enhanced convection of the MJO is located over the Indian Ocean in phases 2-3, the Maritime Continent in phase 5, and the western Pacific in phase 6. Overall, we found that the occurrence probabilities of extreme precipitation and snowfall show different phase changes on the Pacific side and Sea of Japan side. Therefore, instead of combining some MJO phases, the percentage changes for each phase are shown. The probability of observed extreme precipitation (Fig. 6a) saliently increases during phases 2-3 and clearly decreases for phase 6 on the Pacific side, which corresponds to anomalous moist and dry conditions associated with MJO-related southerly and northerly wind anomalies, respectively.

The probability of observed extreme snowfall on the Sea of Japan side (Fig. 7a) remarkably increases for phases 5-6 and decreases for phase 2. This phase change in frequency is consistent with the finding that the probability of extremely cold days increases for phases 5-6 but decreases for phase 2 (Fig. 7c). The results indicate that the increased (decreased) probability of extreme snowfall for phases 5-6 (phase 2) is related to the colder (warmer) temperature condition by the enhanced (weakened) northerly in the corresponding phase of the MJO (Figs. 6b, c). In the Kanto area, the occurrence of snowfall tends to increase in phases 3-5 (Fig. 7a), although it is not necessarily due to extremely cold temperatures (Fig. 7c). The impact of synoptic to large-scale conditions modulated by the MJO on extreme events is described in detail in sections 5 and 6.

d4PDF well captures the changes in the distribution of the probability of extreme precipitation (Fig. 6b) and snowfall (Fig. 7b) with MJO-related circulation and moisture anomalies during the MJO phases as aforementioned observed results. This result indicates that d4PDF successfully reproduces the MJO's influence upon extreme events, and hence, the probability change in extreme events can be quantitatively estimated. We focus on three extreme events that have distinct MJO phase changes: extreme precipitation in the PAC and extreme snowfalls in SJA and Kanto.

Figure 8 shows the probability distribution function (PDFs) of precipitation in PAC and snowfall in SJA and Kanto for MJO phases 1-8 with wintertime climatological PDF during all days in DJF. In addition, histograms and PDF curves in the representative phases that have the most positively or negatively skewed PDFs are also presented with the PDF curves for all days and non-MJO days (MJO amplitude < 1.0) in DJF. For d4PDF, PDFs in PAC precipitation represent a more positively (negatively) skewed distribution in phases 2-4 (phases 6-8) compared to the climatological PDF (Fig. 8d). PDFs in SJA snowfall have more positive skewness in phases 5-6 and skew toward lower values in phases 1-2 and 8 compared with the climatological PDF (Fig. 8e). The Kanto snowfall shows more positively and negatively skewed PDFs in phases 3-5 and phases 1 and 8, respectively (Fig. 8f).

Overall, the phase changes in the skewness of PDFs of rainfall and snowfall for d4PDF are in good agreement with those in the observation (Figs. 8a-c). Although the differences between the observed histograms in MJO phases are unclear (particularly for Kanto snowfall), those between the MJO phases in d4PDF are clearly represented. Therefore, we emphasize that d4PDF enables the occurrence probability in extreme events for MJO phases to be significantly evaluated due to the sufficient sample numbers, although the observation is not enough to determine the significance because of the lack of the sample numbers.

We quantitatively estimate the percentage changes in the probability of extreme event occurrence averaged over the specific areas during MJO phases 1-8 with respect to that of all DJF days from d4PDF (Fig. 9). As the phase change in occurrence probability agrees well between the 95th and 90th percentile threshold values, we describe the case of the 95th threshold. The results indicate that MJO dominantly increases the probability of extreme precipitation in PAC by approximately 40% and 50% in phases 2 and 3, respectively, whereas it clearly decreases the probability by approximately 30% in phase 6 (Fig. 9a). With respect to the extreme snowfall in SJA (Fig. 9c), MJO significantly increases the probability by approximately 20% in phases 4-6 and reduces it by 20-40% in other phases. For Kanto, it is found that the probability of extreme snowfall and precipitation significantly increases by 30-45% in phases 3-5 and by 35-40% in phases 3-4 (Figs. 9b, d), respectively.

To see the effect of extreme temperature drops on extreme snowfall occurrence, the percentage changes in the probability of area-averaged extreme cold events are likewise estimated for SJA and Kanto (Figs. 9e, f). MJO acts to increase the probability of temperature that falls below the 5th percentile during phases 5-6 by approximately 25% and 30% in SJA and Kanto, respectively, and decrease the probability during phases 1-2 and 8 by 30-40% in both areas. The results indicate that the cold extreme brought by the MJO is responsible for the occurrence of extreme snowfall in SJA, whereas abnormally cold temperatures caused by the MJO do not always lead to snowfall events in Kanto.

5. Atmospheric pattern influences on extreme snowfall and rainfall

In this subsection, we explore the large-scale factors that trigger the three extreme events (that is, the snowfalls in SJA and Kanto and precipitation in PAC) and how the MJO influences them. Figures 10 and 11 show composite maps of surface air temperature (SAT), sea-level pressure (SLP), and the large-scale circulation anomalies in the middle-upper troposphere, including the propagation of Rossby wave trains depicted by the wave activity fluxes (Takaya and Nakamura 2001) for the occurrence of the three extremes (more than 95th percentile) during winter all days and those for MJO phases 2-6, respectively, in d4PDF. d4PDF represents very similar patterns of circulation and SAT anomalies in three extreme events and MJO phases and a more widespread significant area to those in the observation (Fig. S3). Therefore, the figures of d4PDF are given for the main text in this section.

5.1 Extreme snowfall in SJA

The anomaly fields during the occurrence of extreme snowfall in SJA (Figs. 10a, b) indicate enhanced cyclonic anomalies centered on northeastern sea of Japan at the surface and over Japan in the middle-upper troposphere. They are accompanied by anomalous anticyclones prevailing over the Eurasian continent north of 50°N and the Arctic Sea at the middle-upper level and all the way to the south of China (20°N) at the surface. These circulation patterns correspond to the Siberian High and Aleutian Low intensifications, leading to the enhancement of the northwesterlies and formation of cold temperature anomalies over East Asia, including Japan (Fig. 10a). Thus, they bring much snowfall to SJA.

It is noteworthy that the anomalous cyclone over Japan with an anticyclone northward over the East Siberia constitute a meridional dipole structure (Fig. 10b). The dipole anomalies develop as part of two Rossby wave trains propagating over the subpolar and subtropical jets as wintertime waveguides. The wave activity fluxes indicate that the Rossby wave train originating from the subtropical anticyclonic anomaly over South Asia (20°-30°N, 100°-120°E) propagates northeastward through Japan, which is an anomalous anticyclone-cyclone-anticyclone pattern (Fig. 10b).

For MJO phases 5-6, the cyclonic anomalies over Japan and the anticyclonic anomalies at middle-upper latitude develop as part of Rossby wave train excited by the MJO anomalous convective heating (Figs. 11b and S3h, i), although these anticyclones center reside around Bering Sea rather than the East Siberia. The result indicates that MJO-related enhanced convection over the Maritime Continent to the western Pacific contributes to the formation of quasi-stationary anomalous circulations with the meridional dipole structure over East Asia to Eastern Siberia, resulting in an increased probability of extreme snowfall occurrence in SJA due to sustained cold anomalies.

5.2 Extreme snowfall in Kanto

The large-scale conditions during extreme snowfall in Kanto are presented for d4PDF (Figs. 10c, d) and observations (Figs. S3c, d). A cyclone in the lower to upper troposphere develops near the south coast of Japan, and an anomalous anticyclone is enhanced over Eastern Siberia and the northwestern Pacific including the Bering Sea. These circulation anomalies develop as part of a northeastward propagating Rossby wave train originating from an anticyclonic anomaly over the Arabian Sea and India (20°N, 60°-100°E) (Figs. 10d and S3d). Zonal dipole circulation anomalies at 20°N (Fig. 10d) have similar patterns to the Matsuno-Gill response (Matsuno, 1966; Gill, 1980) to MJO convective heating in phases 3-5 (Fig. 11b).

Most notably, surface cyclonic patterns clearly form on the sea to the south of Japan in phases 3-5 (Figs. 11a, S3j), accompanied by the middle-level trough over the East Asia (Fig.11b) that is also evident in extreme Kanto snowfall (Fig. 10d). In phase 5, the anticyclonic circulation is similarly produced over the Eastern Siberia to northwestern Pacific, although it is centered to the east of that in extreme events (Figs. 11b, S3j). Upper-level circulation anomalies during the extreme Kanto snowfall have a pronounced inter-event variance over the North Pacific (Fig. S3l), indicating the uncertainty in center location of anticyclonic anomalies. In fact, the observed anomalous anticyclone is most enhanced over the Bering Sea (Fig. S3d).

The results suggest that the enhanced MJO convection over the eastern Indian Ocean to the Maritime Continent encourages a cyclone near the southern coast of Japan, the East Asian trough, and partly an anticyclone over Eastern Siberia and the northwestern Pacific to evolve by producing the Rossby wave train, resulting in an increased likelihood of extreme snowfall in Kanto.

Over the surface (Figs. 10c and S3c), the cold anomalies extend southward and dominate most of Asia, including Japan, accompanied by anomalous anticyclones prevailing over the Eurasian continent. On the other hand, the Siberian high over eastern China is weakened, and cold anomalies over Japan are relatively small in MJO phases 3-4 (Figs. 11a and S3g). We discuss other possible impacts of large-scale atmospheric variability in mid- to high-latitudes associated with pronounced cold anomalies and extreme snowfall in Section 7.

5.3 Extreme rainfall in PAC

The large-scale circulation patterns during the extreme rainfall in PAC (Figs. 10e, f) are mostly opposite in sign to those during the SJA extreme snowfall (Figs.10a, b). Surface cyclonic anomaly develops to the southwest of Japan (Fig. 10e). Comparison of the circulation patterns during the extreme snowfall in Kanto show that an anomalous anticyclone in the notrhwestern Pacific is located relatively southwestward (40°N) and covers Japan, and the middle-upper level cyclonic anomalies dominate over the eastern Siberia (Fig. 10f) that is evidently different from that in Kanto snowfall.

In MJO phases 2-3, the anomalous anticyclone over the Northwestern Pacific and cyclone in the Eastern Siberia are produced similarly to those during extreme rainfall, though the anomalous anticyclone is enhanced more eastward (Figs. 11b, S3k). These anomalous circulations correspond to a poleward dispersion of the Rossby wave train originating from the anticyclonic anomaly over the Arabian Sea and India triggered by MJO. (Fig. 11b).

At the surface (Fig. 10e), the Siberian anomalous high and the corresponding cold anomalies are confined to the north of Asia, which is different from the case of extreme snowfall in Kanto (Fig. 10c). Therefore, the anomalous cyclone near Japan's southern coast and the northwestern Pacific anticyclone can lead to intensified warm and moist southwesterly inflows in Japan due to suppressed cold airmass intrusion, resulting in an increased chance of heavy precipitation rather than snowfall.

6. Dominant factors for the extreme snowfall

The results presented in the previous section show that extreme snowfall events are accompanied by pronounced anticyclonic anomalies over eastern Siberia and the northwestern Pacific, suggesting that atmospheric blocking and associated long-lasting cold air intrusion frequently occur. Furthermore, the cyclone passing through the Pacific Ocean to the south of Japan is evidently important for Kanto snowfall. The MJO produces such anomalous circulations favorable to extreme snowfall occurrences in specified areas over Japan during the respective phase. In this section, to provide physical explanations of the large-scale patterns, we examine the occurrence of atmospheric blocking, cold air intrusion, and cyclone development, which are responsible for extreme snowfall.

6.1 Impact of the atmospheric blocking and CAM inflow

Here, we examine whether extreme events are related to blockings and whether MJO influences the occurrence of extreme events by regulating blockings using the 1-dimensional index (Tibaldi and Molteni, 1990) as shown in Figure 12. Blocking eastern Siberia and the northwestern Pacific promotes cold airmass intrusion from polar regions toward Korea and Japan, leading to favorable conditions for extreme snowfall there (Yamazaki et al. 2015, 2019).

We examine the evolution of the cold air mass (CAM) stream in extreme snowfall events and the influence of the MJO, which is derived from the observation-based analysis (Fig. 13). The CAM flux is defined as the flux of integrated air mass below a threshold isentropic surface (θ = 280 K) in the lower troposphere (Iwasaki et al. 2014) and can quantitatively measure the strength and movement of CAO. Here, day 0 denotes the day of occurrence of extreme snowfall.

6.1.1 Extreme snowfall in SJA

Figure 12a shows anomalies of blocking frequency as a deviation from the wintertime climatology (DJF mean) during the extreme events in the observation. The climatology of the blocking frequency has the largest value in the area of 150°E-160°W and accounts for approximately 13% at a maximum. For extreme snowfall in SJA, the anomalous blocking frequencies evidently increase in the Ural region (50°-80°E) and eastern Siberia (130°-170°E) by up to + 9% and + 12%, respectively.

The CAM flux analysis (Figs. 13a-c) show that polar CAM anomalies originating from the Arctic Ocean anticyclonically rotate along the blocking-type negative potential vorticity (PV) anomaly over eastern Siberia. Subsequently, the predominant CAM flux moves southeastward coupled with a positive PV anomaly over East Asia, resulting in a widespread cooling anomaly around Japan.

6.1.2 Extreme snowfall in Kanto

During extreme snowfall in Kanto (Fig. 12a), the anomalous blocking frequency increases over eastern Siberia and the northwestern Pacific (145°-180°E) by up to + 9%. On the other hand, extreme precipitations in PAC and Kanto are of little relevance to the blocking.

From the analysis of d4PDF (Fig. 12b), similar results are obtained, although the Ural blocking frequency for SJA snowfall is lower than those in the observation. The maximum blocking frequency for SJA snowfall is larger and located further to the west than those for Kanto snowfall. The above results indicate that the formation of blocking with relatively different positions over eastern Siberia and the northwestern Pacific is an important factor causing extreme snowfall in SJA and Kanto.

The CAM stream for the extreme snowfall in Kanto has a partly different path from the snowfall event in SJA (Figs. 13d-f). The polar CAM flux anomalies move southward along the anomalous anticyclone over the Bering Sea and northwestern Pacific and go through the Sea of Okhotsk on day -4 to day -2 (Figs. 13d, e). On day -2 to day 0 (Figs. 13e, f), the southeastward CAM flux toward Japan accompanied by weak positive PV anomaly over East

Asia is unclear in contrast to that during SJA extreme snowfall. On the other hand, the polar CAM flux anomalies are clearly directed southwestward toward Japan along the anomalous anticyclone over the northwestern Pacific. In this way, the oceanic cold northerlies toward Japan largely contribute to Kanto snowfall occurrence, even though they are weaker than those in SJA snowfall.

6.1.3 Impact of MJO

We evaluated the anomalous blocking frequency for MJO phases 1-8 as a deviation from the DJF mean (Figs. 12c, d). The results of observations and d4PDF clearly show that the blocking frequencies significantly increase in eastern Siberia and the northwestern Pacific during MJO phases 5-7 and decrease during phases 1-3, consistent with the finding of Henderson et al. (2016). Figures 12e and f show the change in the probability of blocking for all MJO phases during the SJA and Kanto extreme snowfall events in d4PDF, respectively. Probability changes in blocking frequency averaged over the region of 130°-170°E in SJA extreme snowfall (Fig. 12e) and 145°-180°E in Kanto extreme snowfall (Fig. 12f) increase by 10-20% for MJO phases 5-7 and decrease for other phases with respect to those in all DJF extreme days.

Our results revealed that the quasi-stationary Rossby wave response to MJO heating over the Maritime Continent to the western Pacific significantly contributes to an increase in the probability of extreme snowfall occurrence in SJA (Kanto) during MJO phases 5-6 (phase 5) due to more frequent formation of blocking in eastern Siberia and northwestern Pacific. On the other hand, increased occurrences of extreme snowfall in Kanto and the extreme precipitations during the phases 3-4 are less relevant to the formation of blocking.

The CAM fluxes over East Asia, including Japan, are significantly strengthened by the MJO, when MJO-related convection is active over the Maritime Continent (phase 5) and western Pacific (phase 6) (Figs. 13h, i). In MJO phase 6 (Fig. 13i), the path of CAM from the polar region is similar to that in the SJA extreme snowfall (Fig. 13c). The polar CAM flux anticyclonically moves along MJO-related negative PV anomaly over the eastern Siberia and then cyclonically migrate southeastward accompanied by MJO-induced positive PV anomaly, leading to the cold air outbreak around Japan. Even though the CAM flux and positive PV anomalies over East Asia in phase 5 are relatively weaker than those in phase 6, the CAM intrudes into Japan along the negative PV anomaly formed over the Okhotsk Sea and northwestern Pacific (Fig. 13h). On the other hand, the advection of polar CAM into East Asia is suppressed in phase 3 because the MJO-related anomalous positive (negative) PV dominates over the Bering Sea (the northwestern Pacific) (Fig. 13g).

As the CAM flux cannot be derived from d4PDF datasets, the low-level horizontal temperature advection for the MJO phases is shown in Figs. S4a-f. Northerly (southerly) anomalies dominate over Japan due to the enhancement of cyclonic (anticyclonic) anomalies off the eastern coast of Japan in phase 6 (phase 3) (Figs. S4a-d). Consequently, the anomalous cooling due to cold advection over Japan is intensified in phases 5-6 and suppressed in MJO phases 1-3 and 8 in both the observation and d4PDF (Figs. S4e, f). The phase changes in the cold advection are nearly consistent with those in the observed CAM intensity over Japan (Fig. 13j).

Thus, the MJO acts to promote (suppress) the penetration of the polar CAM into East Asia due to the higher (lower) occurrence frequency of Siberian blocking, which leads to an increase (decrease) in the probabilities of extreme cold temperature and heavy snowfall in SJA and Kanto, when the MJO is located over the eastern Maritime Continent and western Pacific (Indian Ocean).

6.2 Effect of extratropical cyclone development and moisture flux convergence

The occurrences of extreme rainfall in PAC and snowfall in Kanto are attributed to the evolution of cyclones passing near Japan's southern coast, as mentioned in Section 5. Here, we estimate the local deepening rate (LDR) of cyclones defined by Kuwano-Yoshida (2014) to clarify the key process that brings about the occurrence of extreme Kanto snowfall events associated with the MJO, as follows:

$$\mathrm{LDR} = -\frac{p(t+12h)-p(t-12h)}{24}\left|\frac{\sin 60^{\circ}}{\sin\theta}\right| \qquad (2),$$

where p is the SLP, t is the time, and θ is the latitude of the grid point. According to their definition, a cyclone is identified as a rapidly developing cyclone (explosive cyclone) if the LDR exceeds 1 hPa hr^{-1}. Hereafter, we show the LDR anomalies only if the LDR is more than 1.0 hPa hr^{-1}.

Figures 14a-c depict the composites of observed LDR anomalies corresponding to explosive cyclones on day 0. Day 0 denotes the day defined as the extreme events. The LDR anomalies significantly increase from the south coast to the Pacific Ocean side of Japan northeastward during extreme Kanto snowfall and PAC rainfall (Figs. 14b, c), whereas they decrease near Japan during extreme SJA snowfall (Fig. 14a). The variabilities of the LDR anomalies correspond well to those in the anomalous low-level kinetic energy with the synoptic eddies, called "storm track activity", because a synoptic eddy disturbance meridionally conveys heat and moisture to offset the background anomalies (Takahashi et al. 2014).

The composite of the low-level integrated moisture flux convergence and moisture flux is also shown in Figs. 14d-f. During the Kanto snowfall and PAC precipitation events (Figs. 14e, f), the moisture transport from the ocean and moisture flux convergence on the Pacific Ocean side of Japan are intensified due to the enhancement of anomalous cyclones around the south coast of Japan and anticyclones over the northwestern Pacific, respectively.

Figures 15a and b show that the changes in anomalous LDR and storm track activity averaged over the region of 25°-45°N for MJO phases 1-8 in the observation and d4PDF. They evidently increase during MJO phases 3-5 and decrease during phases 1 and 6-8 over the region of 130°-170°E. It is noteworthy that these increased (decreased) phases almost correspond to the increased (decreased) phases of the occurrence probability of extreme snowfall in Kanto (Figs. 8c, f and 9d).

The changes in the observed anomalous moisture flux convergence during the MJO phases are shown in Figs. 15c-e. The southerly moisture flux and its convergence anomalies on the Pacific Ocean side of Japan are intensified (suppressed) during phases 2-4 (phases 5-7) due to the anomalous anticyclone (cyclone) over the northwestern Pacific, which provides favorable (unfavorable) conditions for the occurrence of extreme snowfall in Kanto and precipitation in PAC. A similar result is also found in d4PDF (Figs. S4g-i). The results indicate that the intensification of the MJO-induced moisture flux convergence plays a key role in the occurrence of extreme Kanto snowfall as well as PAC precipitation because it enables a synoptic cyclone passing through the Pacific side of Japan to develop explosively. When the MJO convection is active over the eastern part of the Maritime Continent (phase 5), the increased occurrence of extreme Kanto snowfall is attributed to the intensification of cold air inflow (Figs. 13h, j and S4e, f), which is partly related to the blocking over East Siberia and the northwestern Pacific (Fig. 12f).

7. Conclusions and Discussion

In this study, we investigate the influences of the MJO on the occurrence probability and spatial distribution of wintertime extreme snowfall and precipitation in Japan, which has not been clarified so far, using observational data and a large ensemble of d4PDF global and regional climate datasets. The results show that d4PDF can reproduce the MJO and its teleconnections in the PNA region relatively well compared to those of the multimodel simulations presented by Wang et al. (2020a) and suggest that a large ensemble simulation and SST pattern play an important role in the reproductions.

The primary finding of this study is that the MJO significantly modulates the occurrence probability of extreme snowfalls on the Sea of Japan side (SJA) and Kanto region and extreme precipitation on the Pacific Ocean side (PAC). This result is confirmed by pronounced changes in PDFs skewness of snowfall and precipitation during the MJO phases compared with the wintertime climatological PDF. For the occurrence probabilities of the above three extremes, our analysis indicates that (1) the extreme snowfall in SJA increases by approximately 20% with enhanced MJO convection over the Maritime Continent and western Pacific (phases 4-6), whereas it decreases by 30-40% with the MJO over the western Indian Ocean (phases 1-2), relative to all days in the winter season; (2) the extreme precipitation in PAC increases by 40-50% with the MJO over the Indian Ocean (phases 2-3) and most reduces by approximately 30% with the MJO over the western Pacific (phase 6); and (3) the extreme snowfall in Kanto increases by 30-45% during the MJO over the eastern Indian Ocean and Maritime Continent (phases 3-5).

We examine the relationship of the large-scale circulation patterns responsible for three extreme events with the MJO-induced circulations and present their different triggering mechanisms associated with the MJO. Schematic diagrams are shown in Fig. 16. The active MJO over the Maritime Continent and western Pacific (phases 5-6) intensifies cold air intrusion from Siberia into Japan coupled with the middle-upper-level trough, promoted by more frequent blocking over the East Siberian region, which is conducive to extreme snowfall in SJA (Fig. 16a). When active MJO convection occurs over the Indian Ocean and west of the

Maritime Continent (phases 2-4), MJO-induced moisture flux convergence acts to facilitate the development of explosive south-coast cyclones and storm track activity, which is responsible for extreme snowfall in Kanto and extreme precipitation in PAC (Figs. 16b, c). In addition, the Kanto extreme snowfall in MJO phase 5 is probably attributed to an enhanced cold air inflow associated with the anomalous anticyclone over East Siberia and the northwestern Pacific, which is partly blocking-type high, even though the magnitude of cold air is weaker than the case of extreme snowfall in SJA (Fig. 16b). This study suggests that good representation and monitoring of the MJO help improve the predictability of wintertime extreme precipitation and snowfall in Japan.

Previous studies have indicated that the Arctic Oscillation (AO), which is one of the prominent large-scale atmospheric patterns in the Northern Hemisphere (Thompson and Wallace, 1998), to be an important factor in the occurrence of cold temperature anomalies and cold surges over East Asia (e.g., Jeong and Ho 2005; Song and Wu 2018). Interestingly, the intraseasonal AO pattern is linked to the MJO convective variability during boreal winter (Zhou and Miller 2005; L'Heureux et al. 2008). Song and Wu (2019) showed that the AO-related mid- to high-latitude wave train over Eurasia and the MJO convection-triggered poleward wave train simultaneously contribute to cold temperature anomalies over eastern China. In addition, the wintertime pattern of a warm Arctic-cold continent (WACC; Overland et al. 2011) or warm Arctic-cold Eurasia (WACE; Mori et al. 2014) caused midlatitude extreme cold winters, including East Asia (e.g., Cohen et al. 2014). In this study, we show that the extreme snowfall events in SJA and Kanto are accompanied by mid- to high-latitude wave trains with enhanced and southward extended Siberian highs (Figs. 10, S3).

The occurrences of extreme snowfall in Kanto and precipitation in PAC increase in common during the MJO phases 3-4. They have a common finding that the moisture flux convergence is intensified to promote the development of cyclones along the south coast of Japan, whereas they have distinct differences in the anomalous circulations and temperature advection. (Figs. S4j, k, l, m). In extreme Kanto snowfall (PAC precipitation) for phases 3-4, the anticyclonic anomaly enhanced over the Okhotsk sea and eastern Siberia (over the Northwestern Pacific around 40°N) leads to the advection of northerly cold air (southerly warm air) into Japan. Furthermore, the anticyclonic circulation anomalies at mid- to high-latitude in MJO phases 5-6 are centered to the east of those during the extreme snowfall events (Figs. 16a b). Thus, the result suggests the concurrent influence of large-scale variabilities such as AO and WACC/WACE along with the MJO-induced circulation pattern on extreme snowfall in Japan.

The MJO activity and its teleconnection over the North Pacific and East Asia exhibit pronounced year-to-year variation, which has been modulated by ENSO (Moon et al. 2011, Takahashi et al. 2014) and more strongly attributed to the stratospheric quasi-biennial oscillation (Song et al. 2017, Kim et al. 2020). The combined impact of the MJO and other predominant large-scale teleconnections in mid- to high latitudes, and tropospheric and stratospheric interannual variabilities in the tropics, on extreme events in East Asia including Japan, deserves further investigation in the future to improve subseasonal predictions.

During the last few decades, the observed long-term change in tropical SST anomalies has significantly led to that in the MJO phase residence time (Roxy et al. 2019). As noteworthy finding in previous modeling studies (Wolding et al. 2017, Maloney et al. 2019, Jenny et al. 2021), the extratropical MJO teleconnection especially over the North Pacific is expected to weaken with warming due to the increase in static stability. Furthermore, recent works show that the modeled MJO-teleconnection pattern extends further eastward primarily due to eastward shift of subtropical jet (Zhou et al. 2020) and uncertainty in mean state winds are a primal driver of inter-model uncertainty in future MJO teleconnections (Jenney et al. 2021). Thus, how MJO-related extratropical weather changes with changes in SST pattern and mean state in a warmer climate is an important issue to be further addressed by using a large ensemble of climate and regional models together.

Supplement

Supplement 1 shows scatter diagrams of pattern CCs and relative amplitudes of the skill metrics, and composites of RWS anomalies and subtropical jet. Supplement 2 shows other simulation skills of the MJO teleconnection in d4PDF as additional three metrics. Supplement 3 shows composites of anomalies for three extreme events and MJO phases 2-6 in JRA55. Furthermore, the figure shows composite anomalies during the occurrence days of extreme events in some

MJO phases and inter-member variances of the upper-level circulation anomalies for d4PDF. Supplement 4 shows composites of horizontal temperature advection and vertically integrated moisture flux convergence for the MJO phases. In addition to them, the figure shows differences in the circulation and temperature advection anomalies between during Kanto extreme snowfall and PAC extreme precipitation in some MJO phases.

Acknowledgments

This work was supported by the Integrated Research Program for Advancing Climate Models (TOUGOU) Grant Numbers JPMXD0717935457 and JPMXD0717935561 from the Ministry of Education, Culture, Sports, Science and Technology (MEXT), Japan.

References

1. Abdillah, M. R., Y. Kanno, and T. Iwasaki, 2018: Tropical-extratropical interactions associated with East Asian cold air outbreaks. Part II: Intraseasoanl variation. *J Climate*, **31**, 473-490.
2. Adler, R.F., and Co-authors, 2003: The Version 2 Global Precipitation Climatology Project (GPCP) daily precipitation analysis (1979-present). *J. Hydrometeor*., **4**, 1147-1167.
3. Ahn, M.-S., D. Kim, K. R. Sperber, I.-S. Kang, E. Maloney, D. Waliser, and H. Hendon, 2017: MJO simulations in CMIP5 climate models: MJO skill metrics and process-oriented diagnosis. *Clim. Dynam.,* **49**. 4023-4045.

4. Cohen, J., and Coauthors, 2014: Recent Arctic amplification and extreme mid-latitude weather. *Nat. Geosci*., **7**, 627-637.

5. Deng, Y. and T. Jiang, 2011: Intraseasonal modulation of the North Pacific storm track by tropical convection in boreal winter. *J Climate*, **24**, 1122-1137.

6. Gill. A. E., 1980: Some simple solutions for heat-induced tropical circulation. *Quart. J. Roy. Meteor. Soc*., **106**, 447-462.

7. Guo, Y. and T. Shinoda, 2017: Variations of Northern hemisphere storm track and extratropical cyclone activity associated with the Madden-Julian Oscillation. *J Climate*, **30**, 4799-4818.

8. He, J., H. Lin, and Z. Wu, 2011: Another look at influences of the Madden-Julian Oscullation on the wintertime East Asian weather. *J. Geophys. Res,* **116**, D03109.

9. Henderson, S. A., E. D. Maloney, and E. A. Barnes, 2016: The influence of the Madden-Julian oscillation on Northern Hemisphere winter blocking. *J Climate*, **29**, 4597-4616.

10. Honda, M., A. Yamazaki, A. Kuwano-Yoshida, Y. Kimura, and K. Iwamoto, 2016: Synoptic conditions causing an extreme snowfall event in the Kanto-Koshin district of Japan on 14-15 February 2014. *SOLA*, **12**, 259-264.

11. Iwasaki, T., T. Shoji, Y. Kanno, M. Sawada, M. Ujiie, and K. Takaya, 2014: Isentropic analysis of polar cold airmass streams in the Northern Hemispheric winter. *J. Atmos. Sci.*, **71**, 2230-2243.

12. Jenney, A. M., and D. A. Randall, and E. A. Barnes, 2021: Drivers of uncertainty in future projections of Madden-Julian Oscillation. *Weather Clim. Dynam.,* **2**. 653-673.

13. Jeong, J.-H., and C.-H. Ho, 2005: Changes in occurrence of cold surges over East Asia in association with Arctic oscillation. *Geophys. Res. Lett*., **32**, L14704. doi:10.1029/2005GL023024

14. Jeong, J.-H., C.-H. Ho, and B.-M. Kim, 2005: Influence of the Madden-Julian Oscillation on wintertime surface air temperature and cold surges in East Asia. *J. Geophys. Res*., **110**, D11104.

15. Jeong, J.-H., B.-M. Kim, C.-H. Ho, and Y.-H. Noh, 2008: Systematic variation in wintertime precipitation in East-Asia by MJO-induced extra-tropical vertical motion. *J Climate*, **21**, 788-801.

16. Jiang, X., and Co-authors, 2020: Fifty years of research on the Madden-Julian Oscillation: Recent progress, challenges, and perspectives. *J. Geophys. Res.*, **125**, doi: 10.1029/2019JD030911.

17. Kawase, H., T. Sasai, T. Yamazaki, R. Ito, K. Dairaku, S. Sugimoto, H. Sakai, A. Murata, and M. Nosaka, 2018: Characteristics of synoptic conditions for heavy snowfall in western to northeastern Japan analysed by the 5-km regional climate ensemble experiments. *J. Meteor. Soc. Japan,* **96**, 161-178.

18. Kim, H., S.-W., Son, and C. Yoo, 2020: QBO modulation of the MJO-related precipitation in East Asia. *J. Geophys. Res.*, **125,** e2019JD031929.

19. Kobayashi, S., et al. (2015), The JRA-55 Reanalysis: General specifications and basic characteristics, *J. Meteor. Soc. Japan,* **93**, 5–48.

20. L'Heureux, M. L., and R. W. Higgins, 2008: Boreal winter links between the Madden-Julian Oscillation and the Arctic Oscillation. *J. Climate*, **21**, 3040-3050.

21. Madden, R. A., and P. Julian, 1972: Detection of a global-scale circulation cells in the tropics with a 40-50 day period. *J. Atmos. Sci*., **29**, 1109-1123.

22. Maloney, E. D., A. F. Adames, and H. X. Bui, 2019: Madden-Julian oscillation changes under anthropogenic warming. *Nat. Clim. Change,* **9**, 26–33.

23. Matsueda, S., and Y. Takaya, 2015: The global influence of the Madden-Julian Oscillation on extreme temperature events. *J. Climate*, **28**, 4141-4151.

24. Matsuno, T., 1966: Quasi-geostrophic motions in the equatorial area. *J. Meteor. Soc. Japan,* **44**, 25–42.

25. Matthews, A. J., B. J. Hoskins, and M. Masutani, 2004: The global response to tropical heating in the Madden-Julian Oscillation during Northern winter. *Quart. J. Roy. Meteor. Soc*., **130**, 1991-2011.

26. Mizuta, R., and Co-authors, 2017: Over 5,000 years of ensemble future climate simulations by 60-km global and 20-km regional atmospheric models. *Bull Amer. Meteor. Soc*., **98**, 1383-1398.

27. Moon, J.-Y., B. Wang, and K. -J. Ha, 2011: ENSO regulation of MJO teleconnection. Clim. Dyn., 37, 1133-1149.

28. Moore, R. W., O. Martius, and T. Spengler, 2010: The modulation of the subtropical and extratropical atmosphere in the Pacific basin in response to the Madden-Julian Oscillation. *Mon. Wea. Rev.*, **138**, 2761-2779.

29. Mori, M., M. Watanabe, H. Shiogama, J. Inoue, and M. Kimoto, 2014: Robust Arctic sea-ice influence on the frequent Eurasian cold winters in past decades. *Nat. Geosci*., **7**, 869-873.

30. Overland, J. E., K. R. Wood, and M. Wang, 2011: Warm Arctic-cold continents: Impact of the newly open Arctic Sea. *Polar Res*., **30**, 15787.

31. Park, T.-W., C.-H. Ho, S. Young, and J.-H. Jeong, 2010: Influences of Arctic Oscillation and Madden-Julian Oscillation on cold surges and heavy snowfalls over Korea: A case study for the winter of 2009-2010. *J. Geophys. Res.*, **115**, D23122.

32. Park, T.-W., J. G. Hong, and D.-S. R. Park, 2019: Intra-seasonal characteristics of wintertime extreme cold events over South Korea. *Int. J. Climatology.*, **40**, 2639-2658.

33. Robertson, A. W., A. Kumar, M. Pena, and F. Vitart, 2015: Improving and promoting subseasonal to seasonal prediction, *Bull. Amer. Meteor. Soc.*, **96,** ES49-ES53.

34. Rushley, S. S., D. Kim, and A. F. Adames, 2019: Changes in the MJO under greenhouse gas-induced warming in CMIP5 models. *J Climate*, **32**, 803-821.

35. Ren, H.-L. and P. Ren, 2017: Impact of Madden-Julian Oscillation upon winter extreme rainfall in Southern China: Observations and Predictability in CFSv2. *Atmosphere*, **8**, 192.

36. Roxy, M. K, P. Dasgupta, M. J. McPhaden, T. Suematsu, and C. Zhang, 2019: Twofold expansion of the Indo-Pacific warm pool warps the MJO life cycle. *Nature*, **575**, 647-651.
37. Sakai, K., and R. Kawamura, 2009: Remote response of the East Asian winter monsoon to tropical forcing related to El Niño-Southern Oscillation. *J. Geophys. Res*., **114,** D06105.
38. Sardeshmukh, P. D., and B. J. Hoskins, 1988: The generation of global rotational flow by steady idealized tropical divergence. *J. Atmos. Sci.*, **45**, 1228-1251.
39. Sasai, T., H. Kawase, Y. Kanno, J. Yamaguchi, S. sugimoto, T. Yamazaki, H.sasaki, M. Fujita, and T. Iwasaki, 2019: Future projection of Extreme Heavy snowfall events with a 5-km large ensemble regional climate simulation. *J. Geophys. Res*., **124,** 13975-13990.
40. Seo, K.-H., and H.-J. Lee, 2016: Unraveling the teleconnection mechanisms that induce wintertime temperature anomalies over the Northern Hemisphere continents in response to MJO. *J. Atmos. Sci.*, **73**, 3557-3571.
41. Shoji, T., Y. Kanno, T. Iwasaki, and K. Takaya, 2014: An isentropic analysis of the temporal evolution of East Asian cold air outbreak. *J Climate*, **27**, 9337-9348.
42. Son, S.-W., Y. Lim, C. Yoo, H. H. Hendon, J. Kim, 2017: Stratospheric control of the Madden-Julian Oscillation. *J Climate*, **30**, 1909-1922.
43. Song, L., and R. Wu, 2018: Comparison of intraseasonal East Asian winter cold temperature anomalies in positive and negative phases of the Arctic Oscillation. *J. Geophys. Res,* **123**, 8518-8537.

44. Song, L., and R. Wu, 2019: Combined effects of the MJO and the Arctic Oscillation on the intraseasonal eastern China winter temperature variations. *J. Climate*, **32**, 2295-2311.

45. Stan, C., D. M. Straus, J. S. Frederiksen, H. Lin, E. D. Maloney, and C. Schumacher, 2017: Review of tropical-extratropical teleconnections on intraseasonal time scales. *Rev. Geophysics*, **55**, 902-937.

46. Tachibana, Y., T. Nakamura, and N. Tazou, 2007: Interannual variation in snow-accumulation events in Tokyo and its relationship to the Eurasian pattern. *SOLA*, **3**, 129-132.

47. Takahashi, C., and R. Shirooka, 2014: Storm track activity over the North Pacific associated with the Madden-Julian Oscillation under ENSO conditions during boreal winter. *J. Geophys. Res,* **119**, 10663-10683.

48. Takaya, K., and H. Nakamura, 2001: A formation of a phase-independent wave-activity flux for stationary and migratory quasigeostrophic eddies on a zonally varying basic flow. *J. Atmos. Sci.*, **58**, 608-627.

49. Tibaldi, S., and F. Molteni, 1990: On the operational predictability of blocking. *Tellus*, **42A**, 343-365.

50. Thompson, D. W. J., and J. M. Wallace, 1998: The Arctic oscillation signature in the wintertime geopotential height and temperature fields. *Geophys. Res. Lett.*, **25**, 1297-1300.

51. Ueda, H., A. Kibe, M. Saitoh, and T. Inoue, 2015: Snowfall variations in Japan and its linkage with tropical forcing. *Int. J. Climatol.*, **35**, 991-998.

52. Wallace, J. M., and D. S. Gutzler, 1981: Teleconnections in the geopotential height field during the Northern Hemisphere winter. *Mon. Wea. Rev.,* **109**, 784-812.

53. Wang J. H. Kim, D. Kim, S. A. Henderson, C. Stan, and E. D. Maloney, 2020a: MJO teleconnections over the PNA region in climate models. Part I: Performance- and process-based skill metrics. *J Climate*, **33**, 1051-1067.

54. Wang J. H. Kim, D. Kim, S. A. Henderson, C. Stan, and E. D. Maloney, 2020b: MJO teleconnections over the PNA region in climate models. Part II: Impacts of the MJO and basic state, *J Climate*, **33**, 5081-5101.

55. Wheeler, M., and G. N. Kiladis. 1999: Convectively coupled equatorial waves: Analysis of clouds and temperature in the wavenumber-frequency domain. *J. Atmos. Sci*., **56**, 374-399.

56. Wheeler, M., and H. H. Hendon, 2004: An all-season real-time multivariate MJO index: Development of an index for monitoring and prediction. *Mon. Wea. Rev*., **132**, 1917-1932.

57. Wolding, B. O., E. D. Maloney, S. A. Henderson, and M. Branson, 2017: Climate change and the Madden-Julian Oscillation: a vertically resolved weak temperature gradient analysis. *J. Adv. Model. Earth Syst*., **9**, 307-331.

58. Xavier, P., R. Rahmat, W. K. Cheong, and E. Wallace, 2014: Influence of Madden-Julian Oscillation on Southeast Asia rainfall extremes: Observations and predictability. *Geophys. Res. Lett*., **41**, 4406-4412.

59. Yamashita, Y., R. Kawamura, S. Iizuka, and H. Hatsushika, 2012: Explosively developing cyclone activity in relation to heavy snowfall on the Japan Sea side of central Japan. *J. Meteor. Soc. Japan,* **90**, 275-295.

60. Yamazaki, A., M. Honda, and A. Kuwano-Yoshida, 2015: Heavy snowfall in Kanto and on the Pacific Ocean side of northern Japan associated with western Pacific blocking. *SOLA*, **11**, 59-64.

61. Yamazaki, A., M. Honda, and H. Kawase, 2019: Regional snowfall distributions in a Japan-Sea side area of Japan accociated with jet variability and blocking. *J. Meteor. Soc. Japan,* **97**, 205-226.

62. Yatagai, A., K. Kamiguchi, O. Arakawa, A. Hamada, N. Yasutomi, and A. Kitoh, 2012: APHRODITE: Constructing a Long-term Daily Gridded Precipitation Dataset for Asia based on a Dense Network of Rain Gauges. *Bull. Amer. Meteor. Soc.*, **93,** 1401-1405.

63. Kuwano-Yoshida, A., 2014: Using the local deepening rate to indicate extratropical cyclone activity. *SOLA*, **10**, 199-203.

64. Zhang, C., 2005: Madden-Julian Oscillation. *Rev. Geophys*., **43,** RG2003, doi:10.1029/2004RG000158.

65. Zhang, C., 2013: Madden-Julian Oscillation: Bridging weather and climate. *Bull Amer. Meteor. Soc*., **94**, 1849-1870.

66. Zhang, X. B., L. Alexander, G. C. Hegerl, and Co-authors, 2011: Indices for monitoring changes in extremes based on daily temperature and precipitation data. *Climate Change*, **2**, 851-870.

67. Zhou, S., and A. J. Miller, 2005: The interaction of the Madden-Julian oscillation and the Arctic Oscillation. *J. Climate*, **18**, 143-159.

68. Zhou, W., D. Yang, S.-P. Xie, and J. Ma, 2020: Amplified Madden-Julian oscillation impacts in the Pacific-North America region. *Nat. Clim. Change,* **10**, 654-660.

List of Figures

Fig. 1 (a) RCM domain (shaded area). (b) Topography of Japan represented in the RCM. (c) Three areas defined in the text. Red and blue areas indicate the Sea of Japan side (SJA) and Pacific Ocean side (PAC), respectively. The blue box denotes the Kanto area. The black dotted line in (b, c) represents a borderline between the Sea of Japan side and Pacific Ocean side separated based on the top of altitude.

Fig 2. (a, b) Lag regression of 20-80 day bandpass-filtered precipitation（shaded）and 850-hPa zonal wind (contour, interval 0.3 m s^{-1} in (a) and 0.15 ms^{-1} in (b), red and black lines indicate the positive and negative, respectively) anomalies onto MJO-filtered (i.e., a 20-80-day period and zonal wavenumbers 1-5) precipitation averaged over equatorial Indian Ocean (80°-95°E, 10°S-10°N) in DJF in (a) observation and (b) d4PDF (ensemble mean in 90 members). The anomalies are averaged over 15°S-10°N. White dots and bold lines in (a) denote anomalies significant at 95 % confidence level. The anomalies in (b) indicate the ensemble means of each regression in 90 members. (c, d) Symmetric component of the wavenumber-frequency power spectrum of anomalous equatorial precipitation normalized by background spectrum averaged over 15°S-15°N in (c) observation and (d) d4PDF (one reference member). Black lines represent the dispersion relation of the equatorial Kelvin waves (straight lines) and Rossby waves (curved lines) for equivalent depths of 12, 15, and 50 m.

Fig. 3 Composite of 10-80 day filtered OLR (shaded) and 500-hPa stream function (contour, intervals of 8 × 10^5 m^2 s^{-1}, orange, and green contours indicate the positive and negative, respectively) anomalies at day 0 for MJO phases 1-8 in (a) observation and (b) d4PDF (90 members). Shading indicates statistically significant regions at the 95% confidence level. The yellow box (20°-80°N, 120°E-60°W) in (a) denotes the PNA region.

Fig. 4 Scatter diagrams of pattern CCs of (a) MJO teleconnection over PNA region (TS1) and (b) RWS (TS3) relative to pattern CCs of the MJO (MS1) (x-axis), and relative amplitudes of (c) MJO teleconnection over PNA (TS2) and (d) RWS (TS4) to relative amplitude of the MJO (MS2) (x-axis), averaged over (a, c) day 0-4 lags and (b, d) day 5-9 lags. MS1 and MS2 are calculated from OLR anomaly composites over the region (40°E-140°W, 15°S-15°N). TS1 and TS2 are derived from Z500 anomaly composites over the PNA region. T3 and T4 are calculated from 250-hPa RWS anomaly composites over the region (10°-45°N, 60°-120°W). Gray dots indicate the values for each member of all MJO phases. Purple circles with black numbers and gray bars indicate the ensemble means and ensemble spreads of pattern CCs and amplitudes for each MJO phase, respectively. The navy cross signs exhibit the average of all MJO phases. Red numbers denote the pattern CCs of ensemble means for each MJO phase, with the average of all MJO phases marked by red crosses. The correlation coefficients (r) are calculated from the ensemble means of pattern CCs (purple), pattern CCs of ensemble means (red) for each MJO phase, and all members for all MJO phases (gray). Dabble and single asterisks with numerical values indicate significant correlations exceeding the 99% and 95% confidence levels, respectively.

Fig. 5 Standard deviation (shaded) and mean (white contour, intervals of 3 mm day^{-1} in (a) and 1 cm day^{-1} in (b), respectively) during the winter (DJF): (a) precipitation for 1980-2015 and (b) snowfall for 1980-2018 in Japan based on the observational data. Time series of the monthly mean (open bars) and 5-day running mean (bars) (c) snowfall averaged in the region of SJA, (d) snowfall in Kanto, and (e) precipitation in the PAC during the winter (DJF), 1980-2018. The areas are displayed in Fig. 1c. Monthly (daily) winter-mean climatology is exhibited with thin horizontal solid (dashed) lines. (f) Scatter diagram of observed daily snowfall amount relative to temperature (x-axis) for SJA (blue) and Kanto (red). The correlation coefficients (corr.) are shown in the panel. (g) Time series of DJF-mean anomalies of surface air temperature (red) and precipitable water (green) in JRA55 over Japan (31°-42°N, 131°-142°E). The dashed lines indicate the trends for 1980-2018 in (c, d, g) and 1980-2015 in (e). The values of trends are displayed in each panel. The gray value in (g) is precipitable water. The asterisk denotes significance value exceeding 95% confidence level.

Fig. 6 Percentage changes (shaded) in the probability of extreme precipitation events exceeding the 95th percentile values with respect to winter climatological PDF for the MJO phases

(phases 2, 3, 5 and 6) for (a) observation and (b) d4PDF. Contours represent the composite of 10-80 day filtered 850-hPa specific humidity anomalies. Contour intervals are (a) 8 and (b) 4 $\times 10^{-5}$ kg kg^{-1}. Solid (dotted) lines indicate positive (negative) values. Gray lines represent zero value. The vectors show the composite of 10-80 day filtered 850-hPa wind anomalies.

Fig. 7 Same as Fig. 6 but for the percentage changes in the probability of extreme (a, b) snowfall exceeding the 95th percentile and (c) surface temperature below the 5th percentile values for (a, c) observation and (b) d4PDF. Contours represent 10-80 day filtered 850-hPa stream-function in (a, b) and 850-hPa temperature anomalies in (c). Contour intervals are (a) 4×10^5 m^2 s^{-1}, (b) 3×10^5 m^2 s^{-1}, and (c) 0.2 K.

Fig. 8 Probability distribution (box plots) of (a, d) precipitation in PAC, (b, e) snowfall in SJA, and (c, f) snowfall in Kanto for MJO phases 1-8 and all days (DJF) in the upper parts for (a-c) observations and (d-f) d4PDF. Red (blue) indicates the MJO phases with a more positively (negatively) skewed distribution than that for all days (DJF). Histograms of the MJO phases with the most positively (red line) and negatively (blue line) skewed distributions are shown in the lower parts. The PDF curves are also plotted for d4PDF. For Kanto snowfall, two phases are combined due to the infrequent occurrence in (c, f). The black line and black dashed line denote PDFs for all days in DJF and non-MJO (MJO amplitude < 1), respectively. The vertical dotted lines indicate the 95th percentile values.

Fig. 9 Area-averaged percentage changes in the probability of extreme (a) precipitation in PAC, (b) precipitation in Kanto, (c) snowfall in SJA, (d) snowfall in Kanto, (e) temperature in SJA, and (f) temperature in Kanto for the MJO phases with respect to winter climatological PDF in d4PDF. The thresholds of extremes for precipitation and snowfall (temperature) are the 90th and 95th (5th and 10th) percentile values during winter all days.

Fig. 10 Composites of (a, c, e) surface air temperature (shaded) and sea level pressure (contour, intervals of 1 hPa, red and black lines indicate the positive and negative, respectively) anomalies and (b, d, f) 500-hPa geopotential height (shaded), 250-hPa stream function anomalies (contour, intervals of 2×10^6 m^2 s^{-1}), and 250-hPa wave activity flux vectors for extreme (a, b) snowfall in SJA, (c, d) snowfall in Kanto, and (e, f) precipitation in PAC at the day of occurrence of each extreme event (day 0) for d4PDF. Dots indicate statistically significant regions at the 95% confidence level.

Fig. 11 Same as Fig. 10 but for composites of anomalies at day 0 during MJO phases 2-6.

Fig. 12 (a, b) Climatology (gray) and anomalies of blocking frequency for four extreme events (SJA snowfall; red, Kanto snowfall; blue, PAC precipitation; yellow, Kanto precipitation; green) during the winter in (a) observation and (b) d4PDF. (c, d) Same as (a) and (b) but for the blocking frequency anomalies in MJO phases, respectively. (e, f) Percentage changes of blocking frequency anomalies for extreme snowfall events in (e) SJA and (f) Kanto for MJO phases to those in winter all days, averaged over the region of 130°-170°E (hatching area in (b)) and 145°-180°E (gray shaded area in (b)), respectively.

Fig. 13 Lag composite of 850-hPa temperature and (shaded), potential vorticity on 320 K surface (contour), and cold air mass (CAM) flux (vector, green arrows) anomalies for (a-c) SJA extreme snowfall event, (d-f) Kanto extreme snowfall event, and (g-i) MJO phases 3, 5, 6. Shading is displayed only for negative temperature anomaly. Contour intervals are (a-c) 0.2, (d-f) 0.15, and (g-i) 0.1 K m^2 $kg^{-1}s^{-1}$. The red and blue lines indicate the positive and negative values, respectively. (j) CAM flux intensity averaged over Japan (yellow rectangle) for MJO phases.

Fig. 14 Composites of observed (a-c) LDR (shaded) and 850-hPa kinetic energy (KE) of synoptic eddies (contour, an interval of 1.5 m^2 s^{-2}, red and black lines indicate positive and negative values, respectively, 9-day running mean) anomalies for extreme (a) snowfall events in SJA, (b) snowfall events in Kanto, and (c) precipitation events in PAC. (d-f) Same as (a-c) but for vertical-integrated (925-500 hPa) moisture flux convergence (shaded) and vertical-integrated (925-700 hPa) moisture flux (vector). Dots indicate statistically significant regions at the 95% confidence level.

Fig. 15 Composites of (a, b) LDR (shaded) and 850-hPa KE of synoptic eddy (contour, interval of (a) 0.5 m^2 s^{-2} and (b) 0.3 m^2 s^{-2}, red and black lines indicate positive and negative values, respectively, 9-day running mean) averaged over the region of 25°-45°N in the MJO phases for (a) observation and (b) d4PDF. Composite of observed (c, d) vertically integrated (925-500-hPa) moisture flux convergence (shaded), precipitation anomalies (contour, an interval of 0.3 mm day^{-1}, red and black lines indicate positive and negative values, respectively), and vertically integrated (925-700-hPa) moisture flux (vector) in (c) MJO phases 2, 3, 4 and (d) MJO phase 6, and (e) vertically integrated (925-500-hPa) moisture flux convergence averaged over Japan (gray rectangle in (c)) in MJO phases.

Fig. 16 Schematic illustrations of large-scale circulations related to the MJO for (a) extreme snowfall in SJA, (b) extreme snowfall in Kanto, and (c) extreme precipitation in PAC. The orange and purple shaded areas indicate anticyclonic circulations (Ae) and cyclonic circulations (Ce) anomalies, respectively, at the middle-upper level during the occurrence of each extreme event. The red and blue closed curves show anticyclonic circulations (Am) and cyclonic circulations (Cm) anomalies, respectively, at the middle-upper level, in MJO (a) phases 5-6, (b) phase 5 (Am) and phases 4-5 (Cm), and (c) phases 2-4, which is responsible for increased occurrence of each extreme event. The green shaded areas (Ce,m) in (b, c) indicate developing surface cyclones on the sea to the south of Japan formed in MJO (b) phases 3-5 and

(c) phases 2-4. The blue and red arrows denote the enhanced CAM flux and vertical-integrated moisture flux anomalies, respectively, which are contributing factors for the occurrence of extreme events. The black shadings show the occurrence areas of each extreme event.

Fig. 1

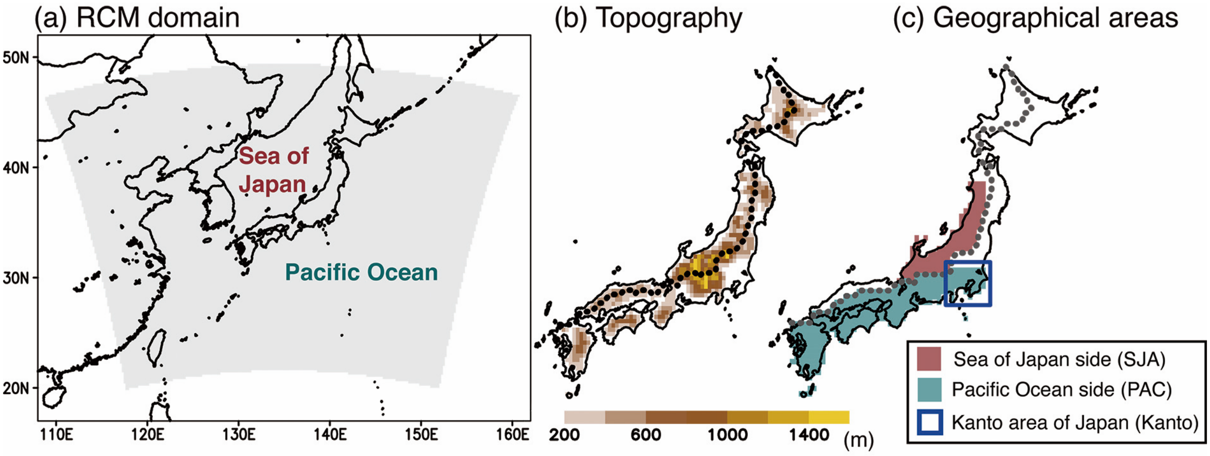

(a) RCM domain
(b) Topography
(c) Geographical areas
Sea of Japan
Pacific Ocean
50N
40N
30N
20N
110E
120E
130E
140E
150E
160E
200
600
1000
1400
(m)
Sea of Japan side (SJA)
Pacific Ocean side (PAC)
Kanto area of Japan (Kanto)

Fig. 2

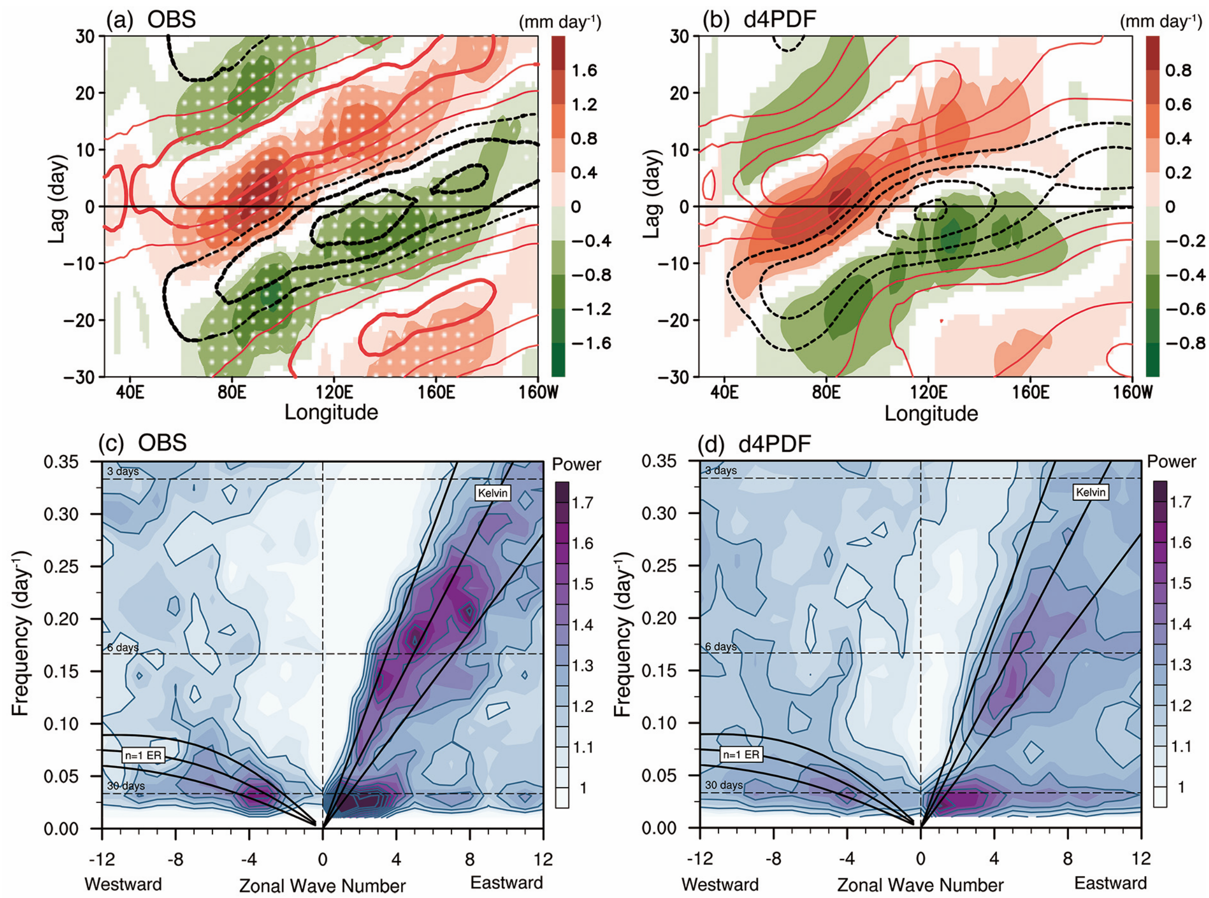

(a) OBS
(mm day⁻¹)
(b) d4PDF
Lag (day)
Longitude
40E
80E
120E
160E
160W
(c) OBS
(d) d4PDF
Power
Frequency (day⁻¹)
3 days
6 days
30 days
Kelvin
n=1 ER
Westward
Zonal Wave Number
Eastward

Fig. 3

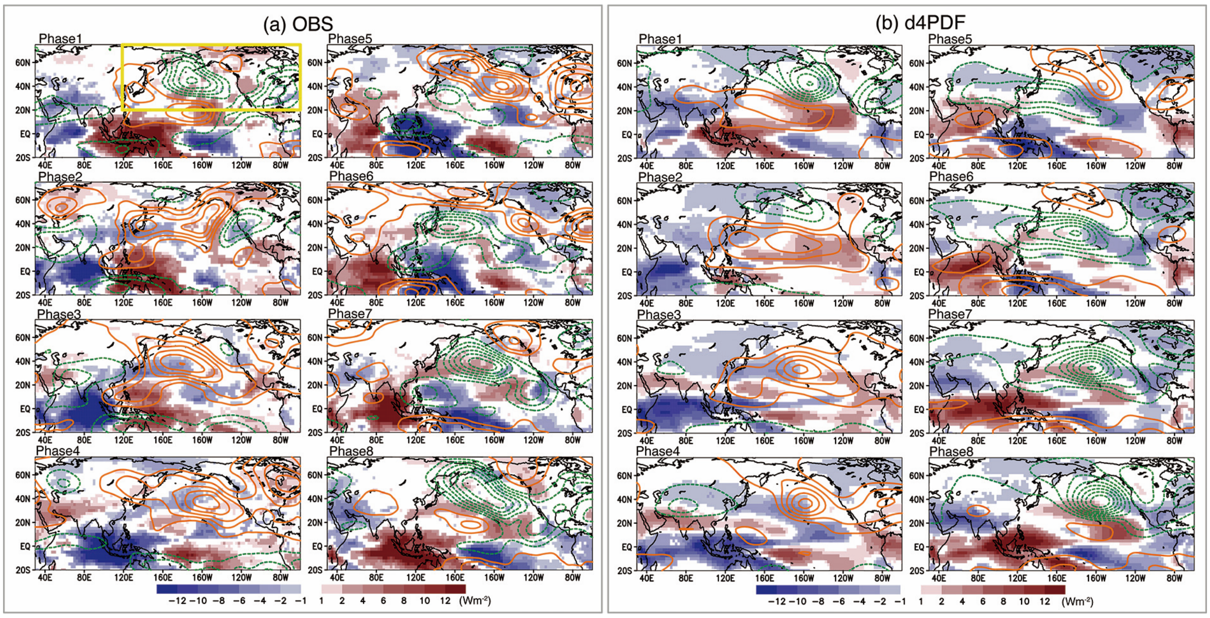
(a) OBS
(b) d4PDF
Phase1
Phase2
Phase3
Phase4
Phase5
Phase6
Phase7
Phase8
60N
40N
20N
EQ
20S
40E
80E
120E
160E
160W
120W
80W
−12 −10 −8 −6 −4 −2 −1 1 2 4 6 8 10 12 (Wm⁻²)

Fig. 4

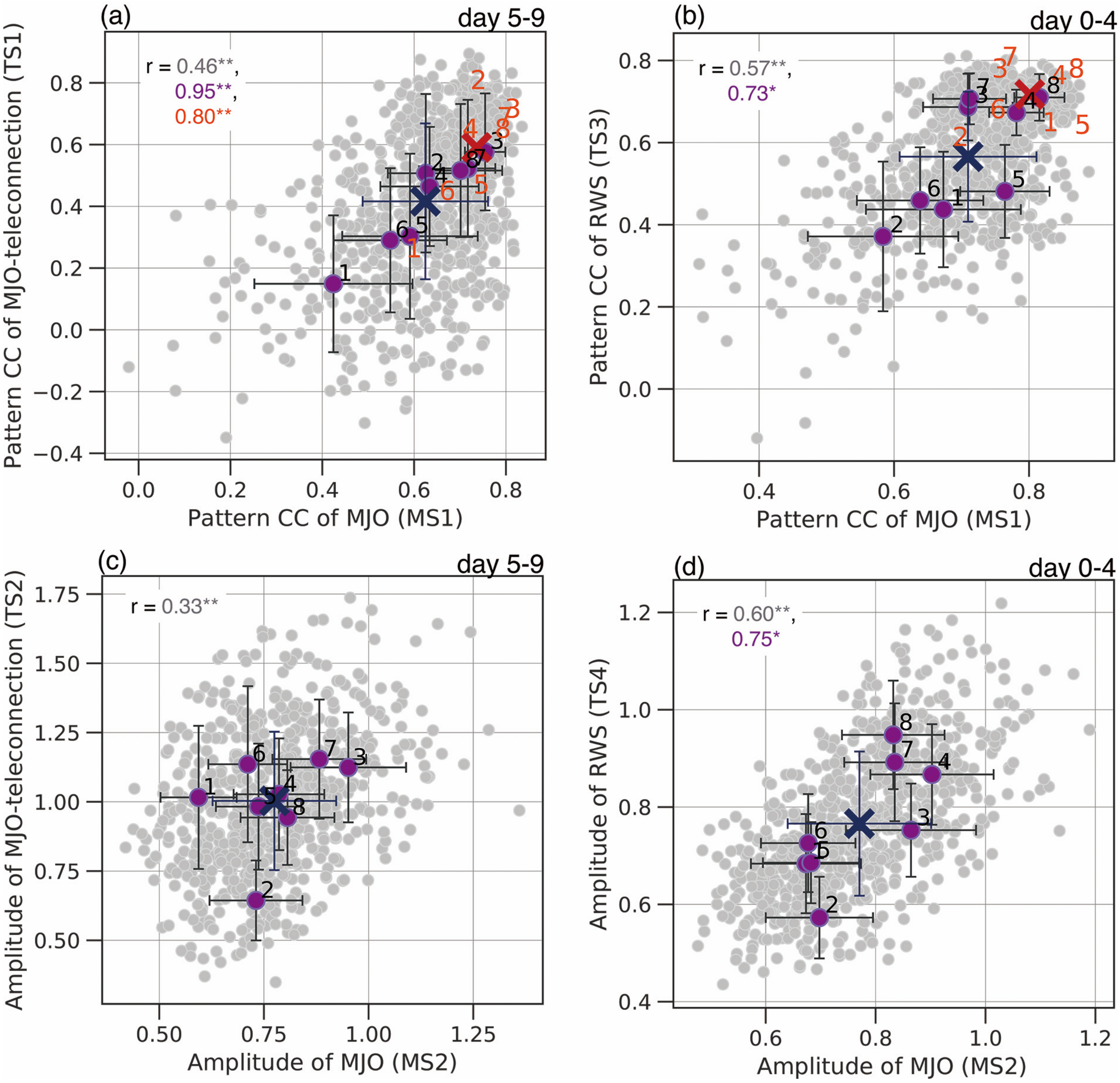
(a)
day 5-9
r = 0.46**,
0.95**,
0.80**
Pattern CC of MJO-teleconnection (TS1)
Pattern CC of MJO (MS1)
(b)
day 0-4
r = 0.57**,
0.73*
Pattern CC of RWS (TS3)
Pattern CC of MJO (MS1)
(c)
day 5-9
r = 0.33**
Amplitude of MJO-teleconnection (TS2)
Amplitude of MJO (MS2)
(d)
day 0-4
r = 0.60**,
0.75*
Amplitude of RWS (TS4)
Amplitude of MJO (MS2)

Fig. 5

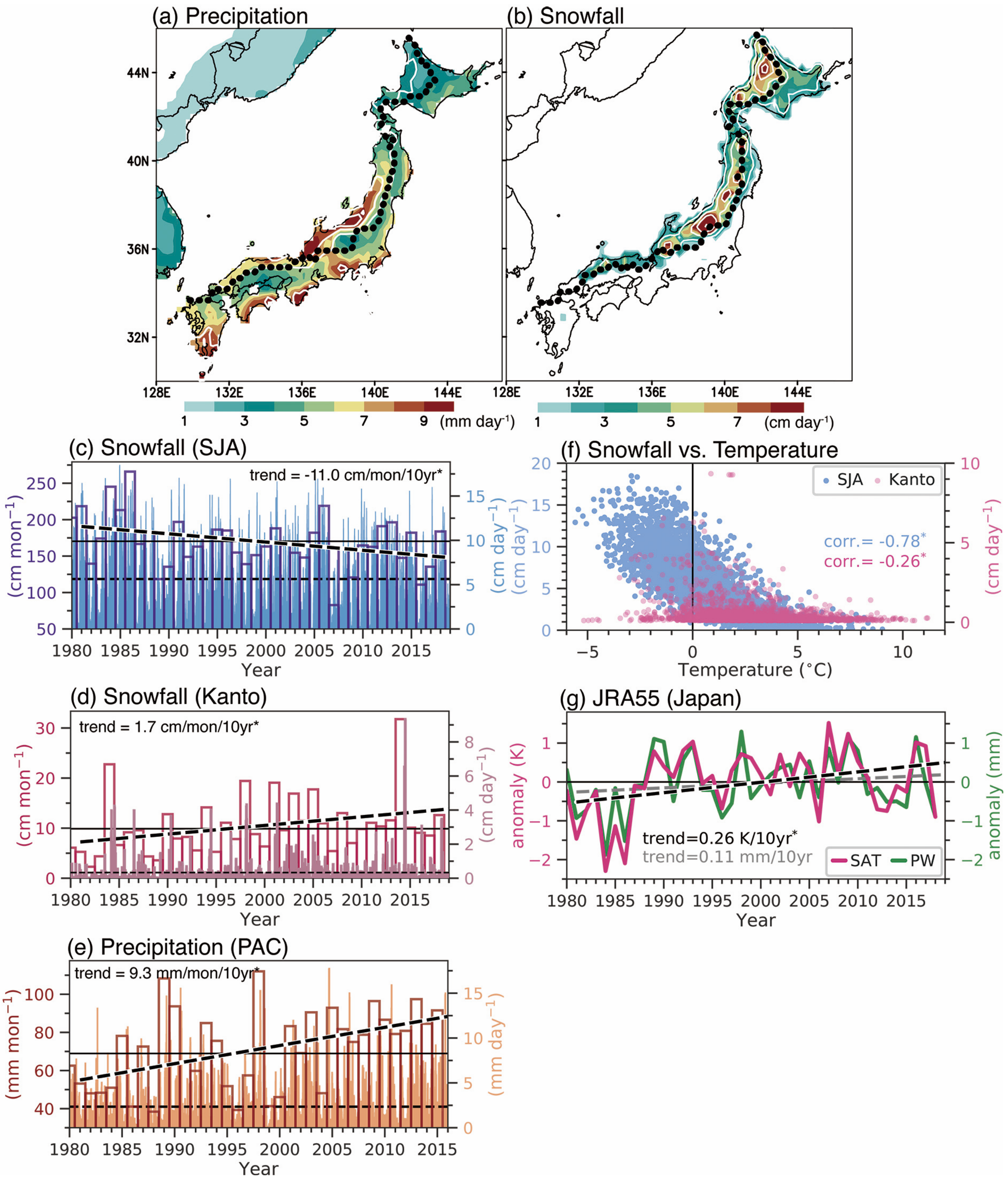

(a) Precipitation
(b) Snowfall
44N
40N
36N
32N
128E
132E
136E
140E
144E
1 3 5 7 9 (mm day⁻¹)
1 3 5 7 (cm day⁻¹)
(c) Snowfall (SJA)
trend = -11.0 cm/mon/10yr*
(cm mon⁻¹)
(cm day⁻¹)
Year
(d) Snowfall (Kanto)
trend = 1.7 cm/mon/10yr*
(cm mon⁻¹)
(cm day⁻¹)
Year
(e) Precipitation (PAC)
trend = 9.3 mm/mon/10yr*
(mm mon⁻¹)
(mm day⁻¹)
Year
(f) Snowfall vs. Temperature
SJA
Kanto
corr.= -0.78*
corr.= -0.26*
(cm day⁻¹)
Temperature (°C)
(g) JRA55 (Japan)
trend=0.26 K/10yr*
trend=0.11 mm/10yr
SAT
PW
anomaly (K)
anomaly (mm)
Year

Fig. 6

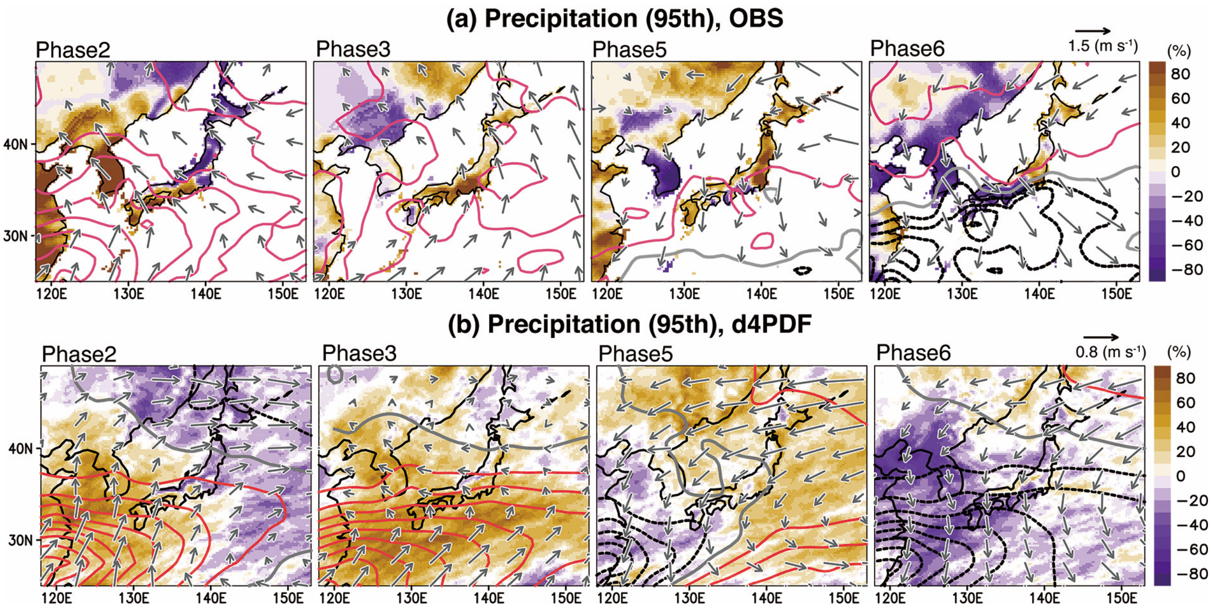
(a) Precipitation (95th), OBS
Phase2
Phase3
Phase5
Phase6
1.5 (m s-1)
(%)
80
60
40
20
0
−20
−40
−60
−80
40N
30N
120E
130E
140E
150E
(b) Precipitation (95th), d4PDF
Phase2
Phase3
Phase5
Phase6
0.8 (m s-1)
(%)
80
60
40
20
0
−20
−40
−60
−80
40N
30N
120E
130E
140E
150E

1039 Fig. 7

1040

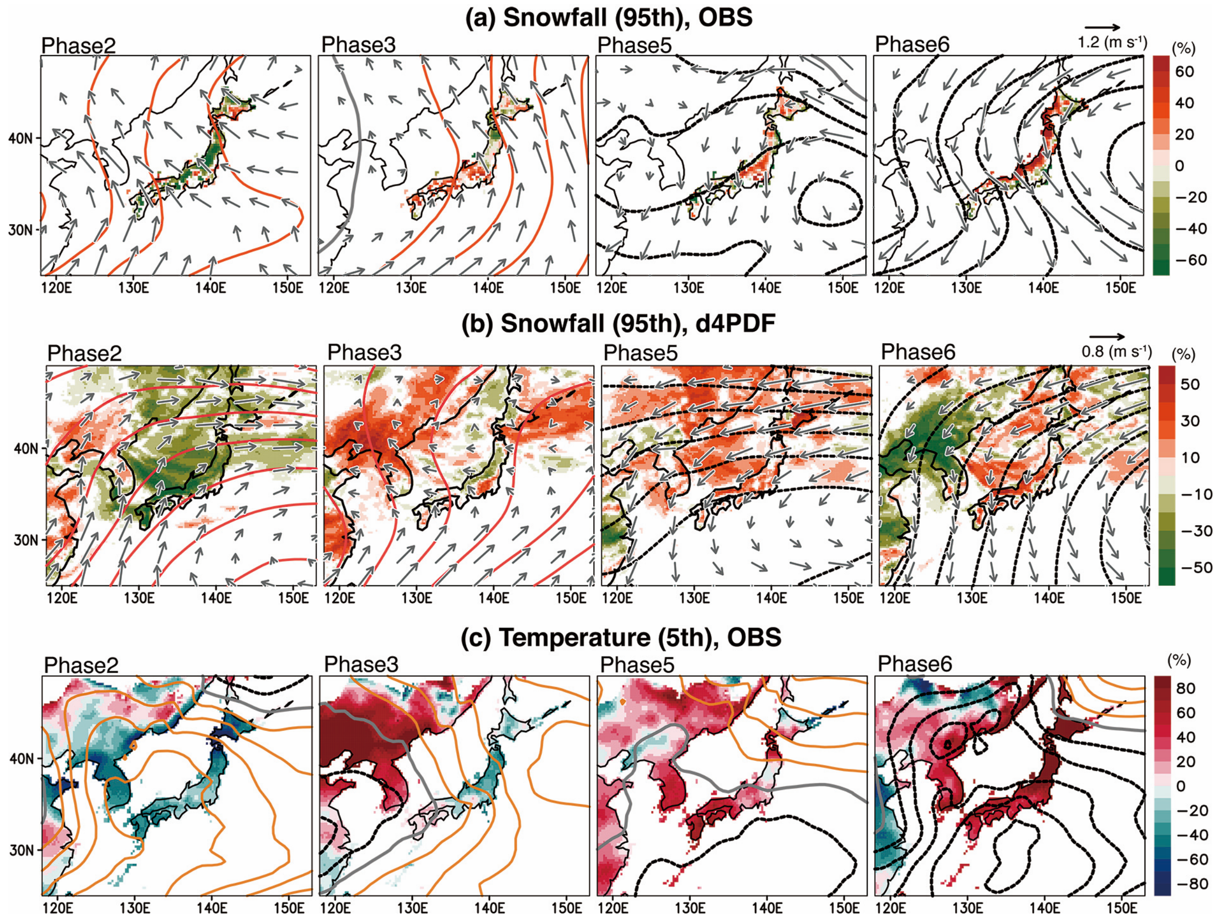

1041

1042

1043 Fig. 8

1044

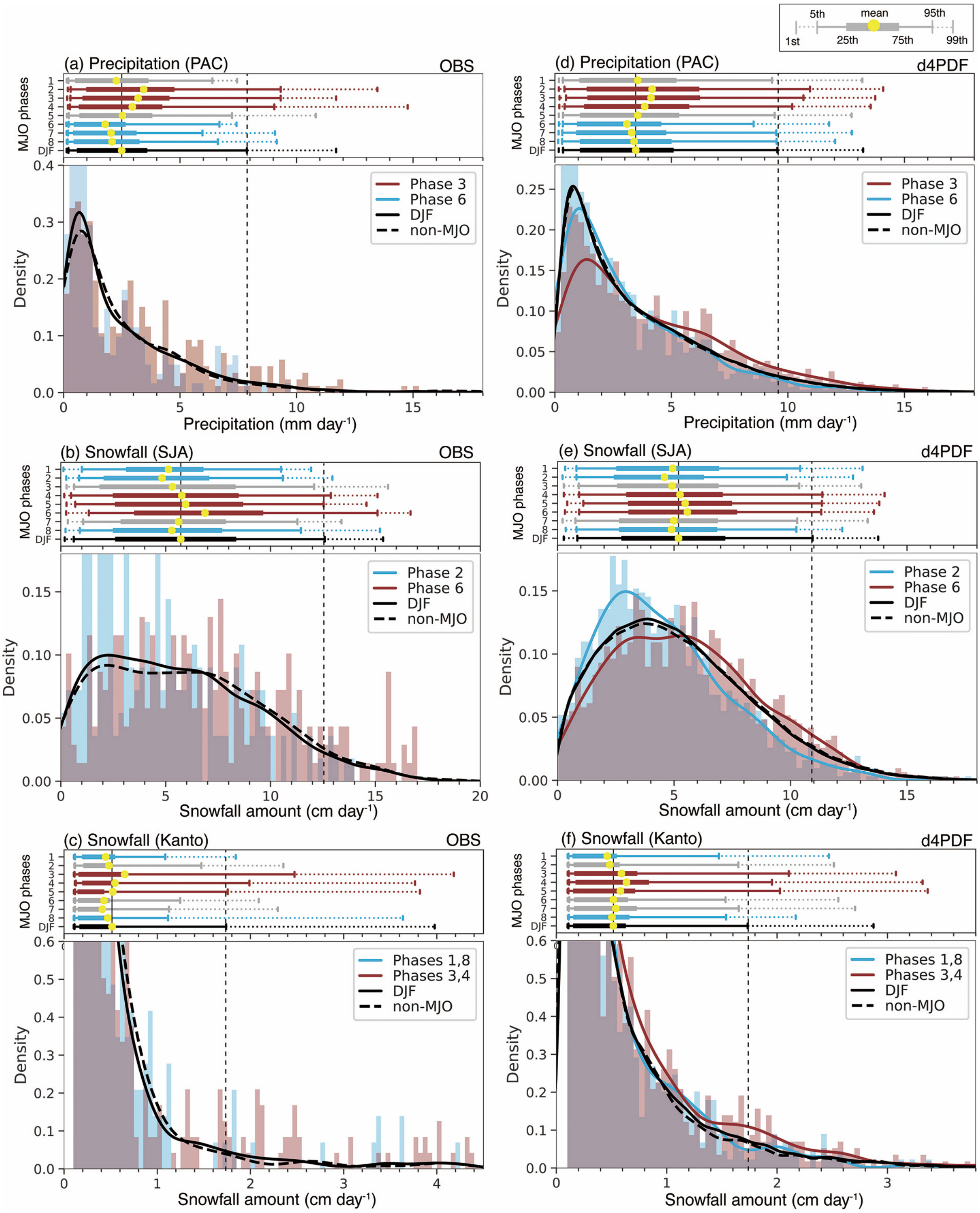

1045

1046

Fig. 9

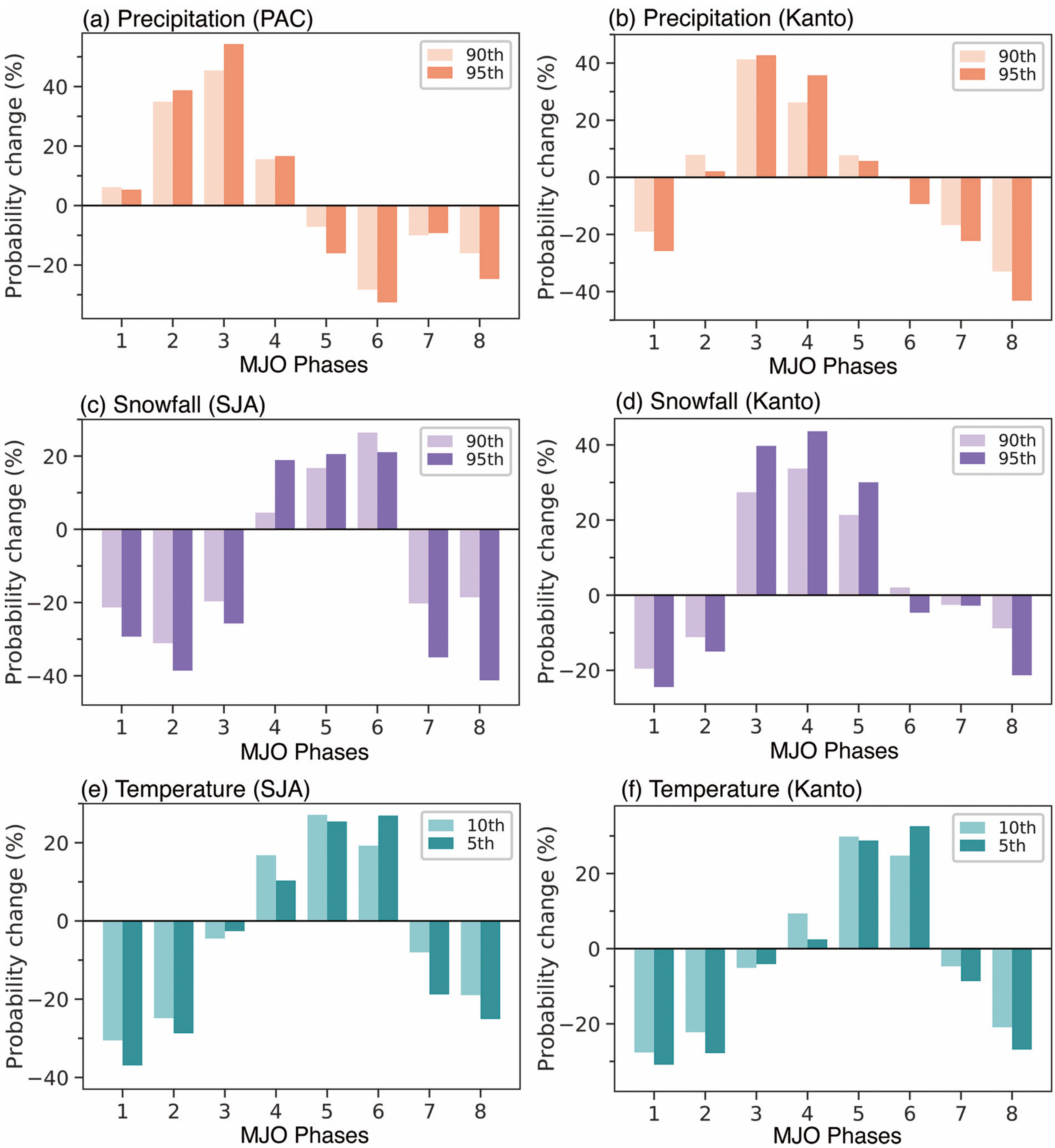

(a) Precipitation (PAC)
(b) Precipitation (Kanto)
(c) Snowfall (SJA)
(d) Snowfall (Kanto)
(e) Temperature (SJA)
(f) Temperature (Kanto)
90th
95th
10th
5th
Probability change (%)
MJO Phases

Fig. 10

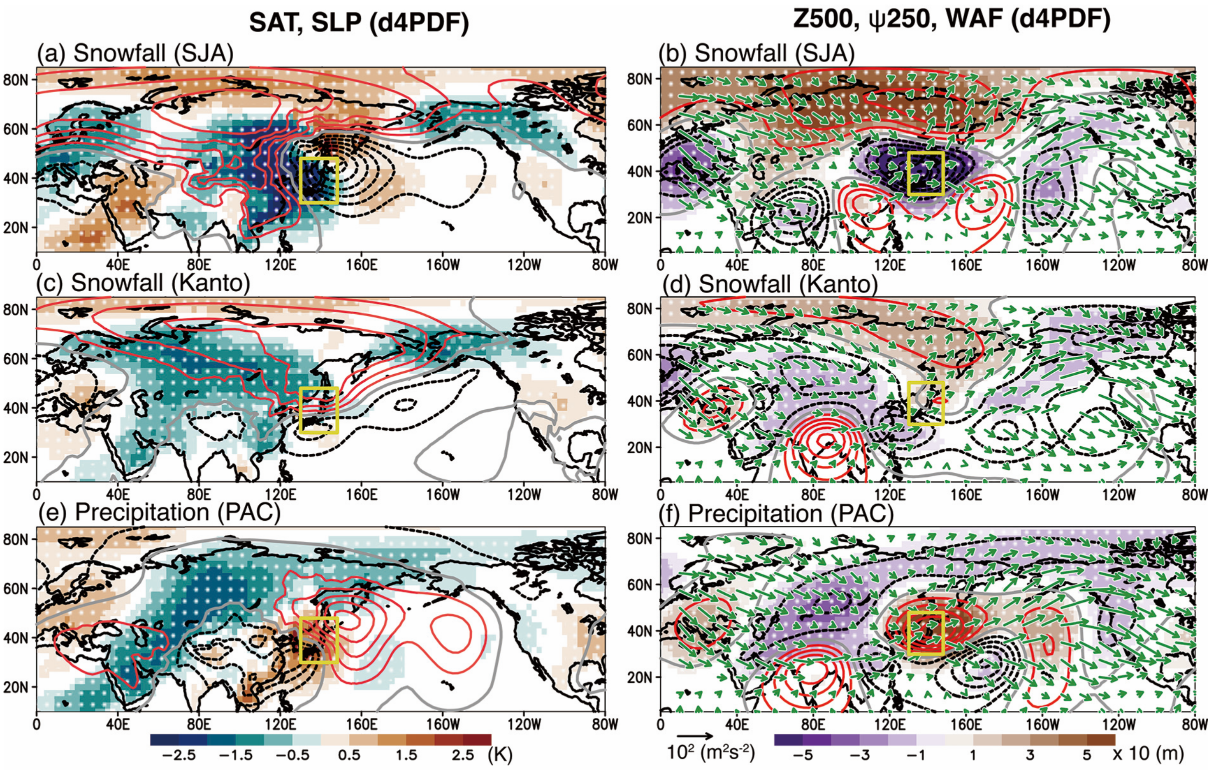
SAT, SLP (d4PDF)
Z500, ψ250, WAF (d4PDF)
(a) Snowfall (SJA)
(b) Snowfall (SJA)
(c) Snowfall (Kanto)
(d) Snowfall (Kanto)
(e) Precipitation (PAC)
(f) Precipitation (PAC)
80N
60N
40N
20N
0
40E
80E
120E
160E
160W
120W
80W
−2.5 −1.5 −0.5 0.5 1.5 2.5 (K)
10² (m²s⁻²)
−5 −3 −1 1 3 5 x 10 (m)

Fig. 11

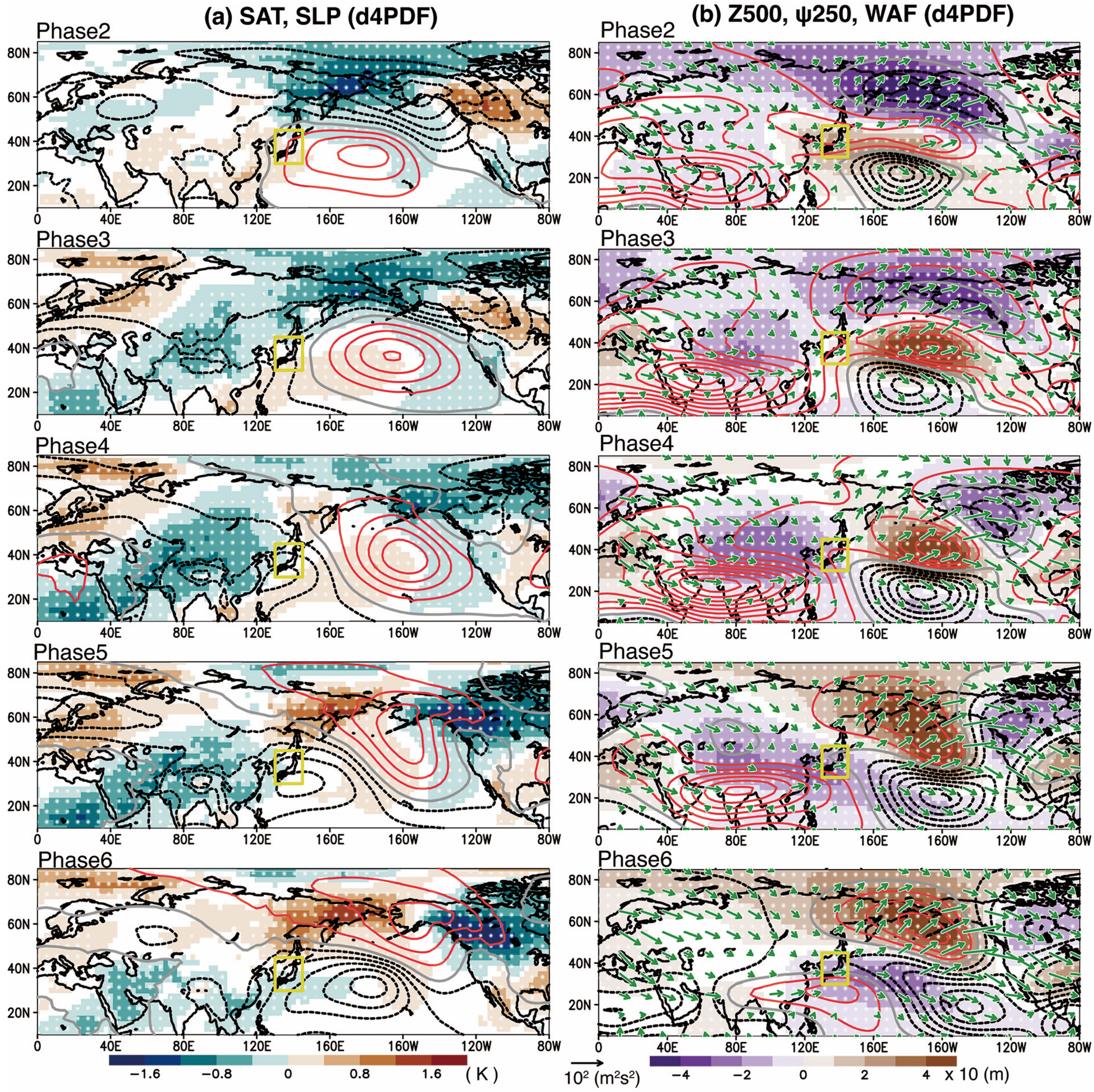

(a) SAT, SLP (d4PDF)
(b) Z500, ψ250, WAF (d4PDF)
Phase2
Phase3
Phase4
Phase5
Phase6
80N
60N
40N
20N
0
40E
80E
120E
160E
160W
120W
80W
−1.6
−0.8
0
0.8
1.6
(K)
10² (m²s²)
−4
−2
0
2
4
x 10 (m)

1058 Fig. 12

1059

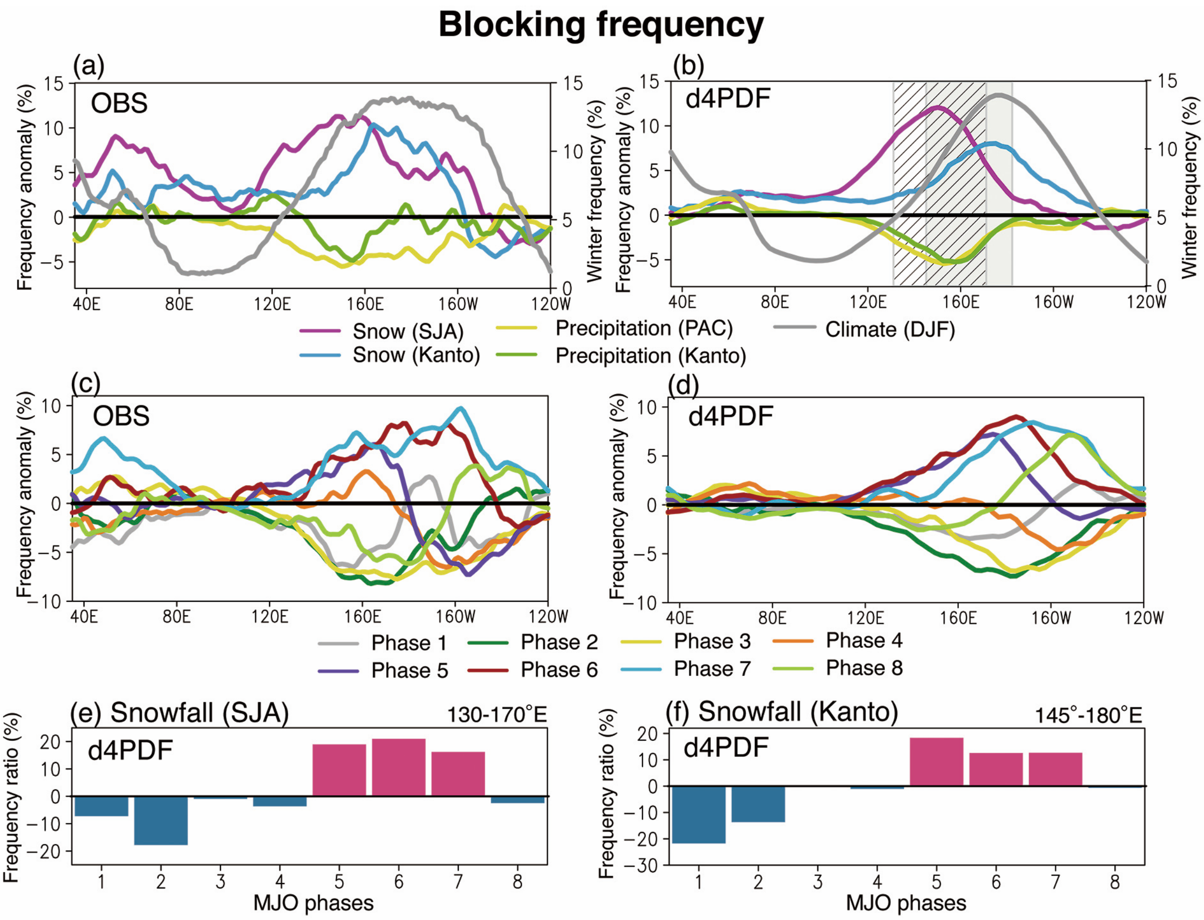

1060

1061

Fig. 13

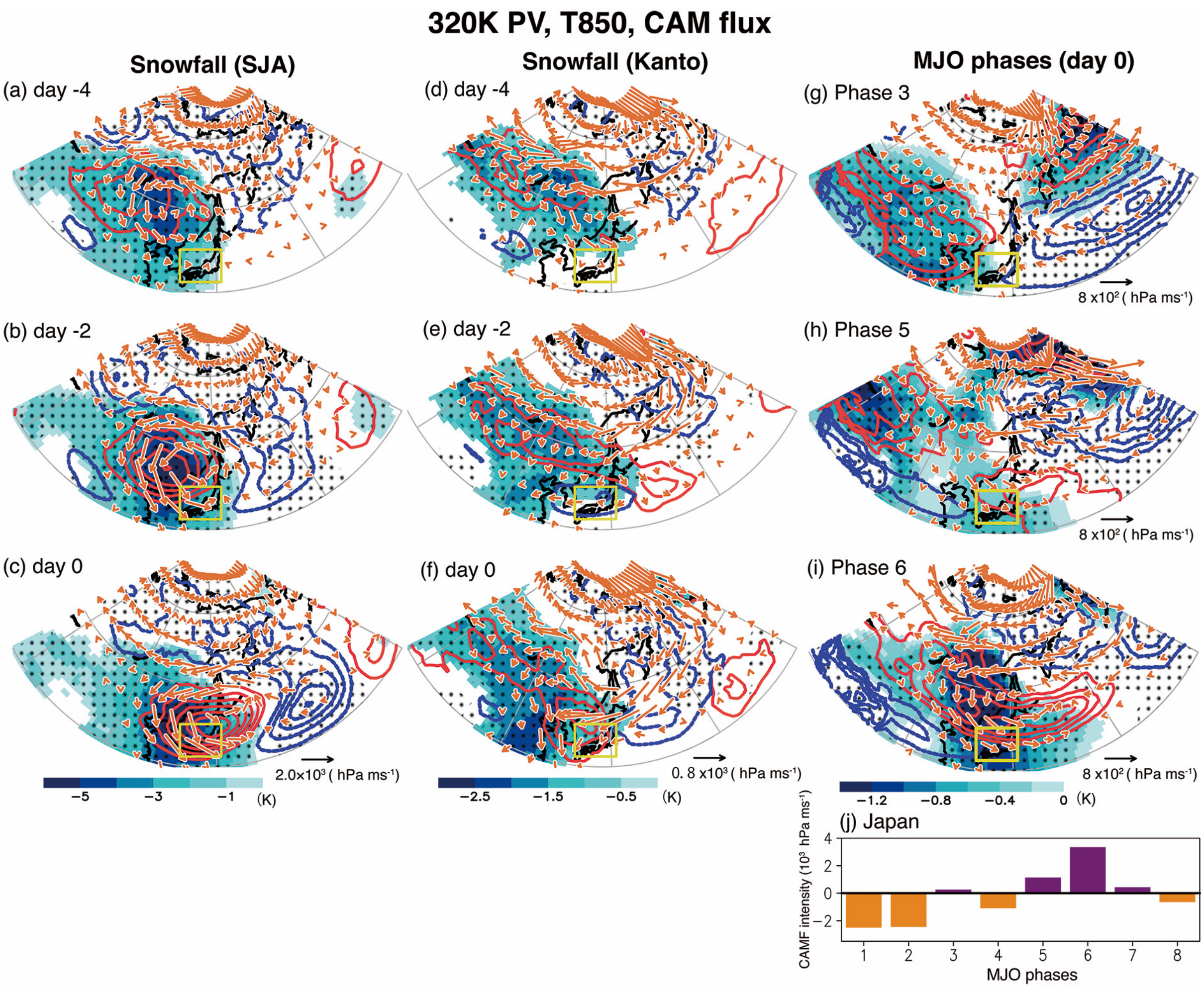
320K PV, T850, CAM flux
Snowfall (SJA)
Snowfall (Kanto)
MJO phases (day 0)
(a) day -4
(b) day -2
(c) day 0
(d) day -4
(e) day -2
(f) day 0
(g) Phase 3
(h) Phase 5
(i) Phase 6
8 x10² (hPa ms⁻¹)
8 x10² (hPa ms⁻¹)
2.0×10³ (hPa ms⁻¹)
0. 8 x10³ (hPa ms⁻¹)
8 x10² (hPa ms⁻¹)
−5 −3 −1 (K)
−2.5 −1.5 −0.5 (K)
−1.2 −0.8 −0.4 0 (K)
(j) Japan
CAMF intensity (10³ hPa ms⁻¹)
4 2 0 −2
1 2 3 4 5 6 7 8
MJO phases

Fig. 14

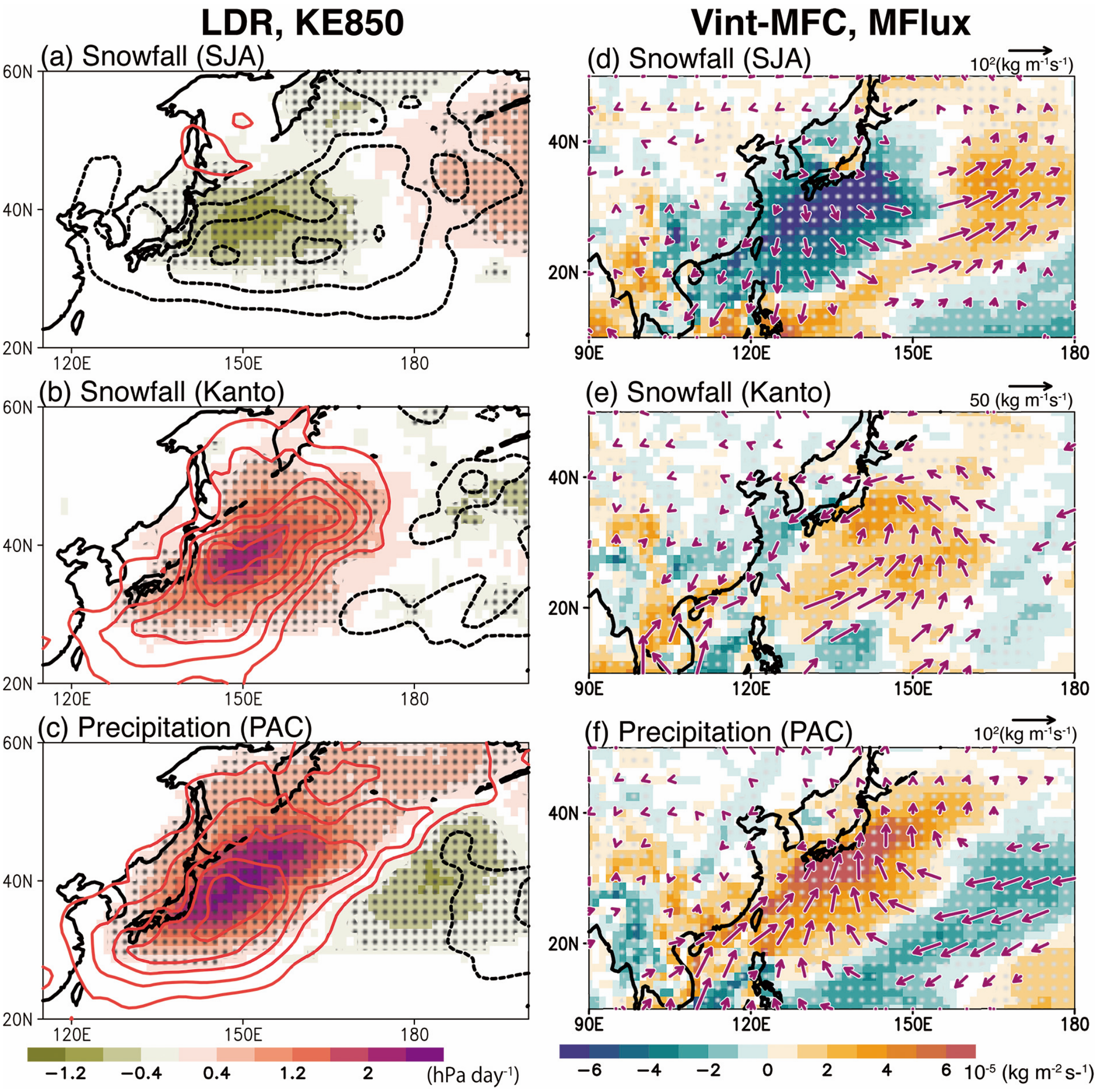

LDR, KE850
Vint-MFC, MFlux
(a) Snowfall (SJA)
(b) Snowfall (Kanto)
(c) Precipitation (PAC)
(d) Snowfall (SJA)
(e) Snowfall (Kanto)
(f) Precipitation (PAC)
10²(kg m⁻¹s⁻¹)
50 (kg m⁻¹s⁻¹)
60N
40N
20N
120E
150E
180
90E
−1.2 −0.4 0.4 1.2 2 (hPa day⁻¹)
−6 −4 −2 0 2 4 6 10⁻⁵ (kg m⁻² s⁻¹)

Fig. 15

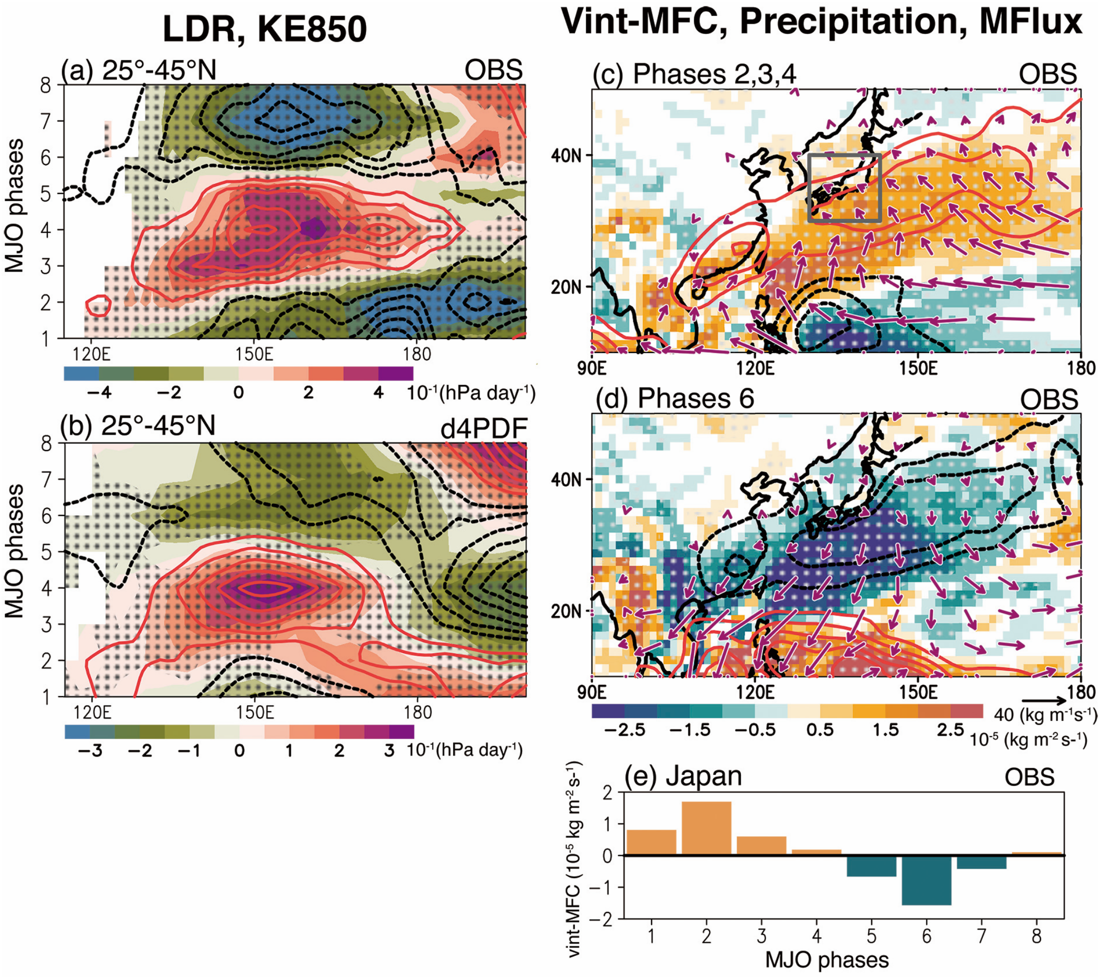
LDR, KE850
(a) 25°-45°N
OBS
MJO phases
10⁻¹(hPa day⁻¹)
(b) 25°-45°N
d4PDF
Vint-MFC, Precipitation, MFlux
(c) Phases 2,3,4
(d) Phases 6
40 (kg m⁻¹s⁻¹)
10⁻⁵ (kg m⁻² s⁻¹)
(e) Japan
vint-MFC (10⁻⁵ kg m⁻² s⁻¹)
MJO phases

Fig. 16

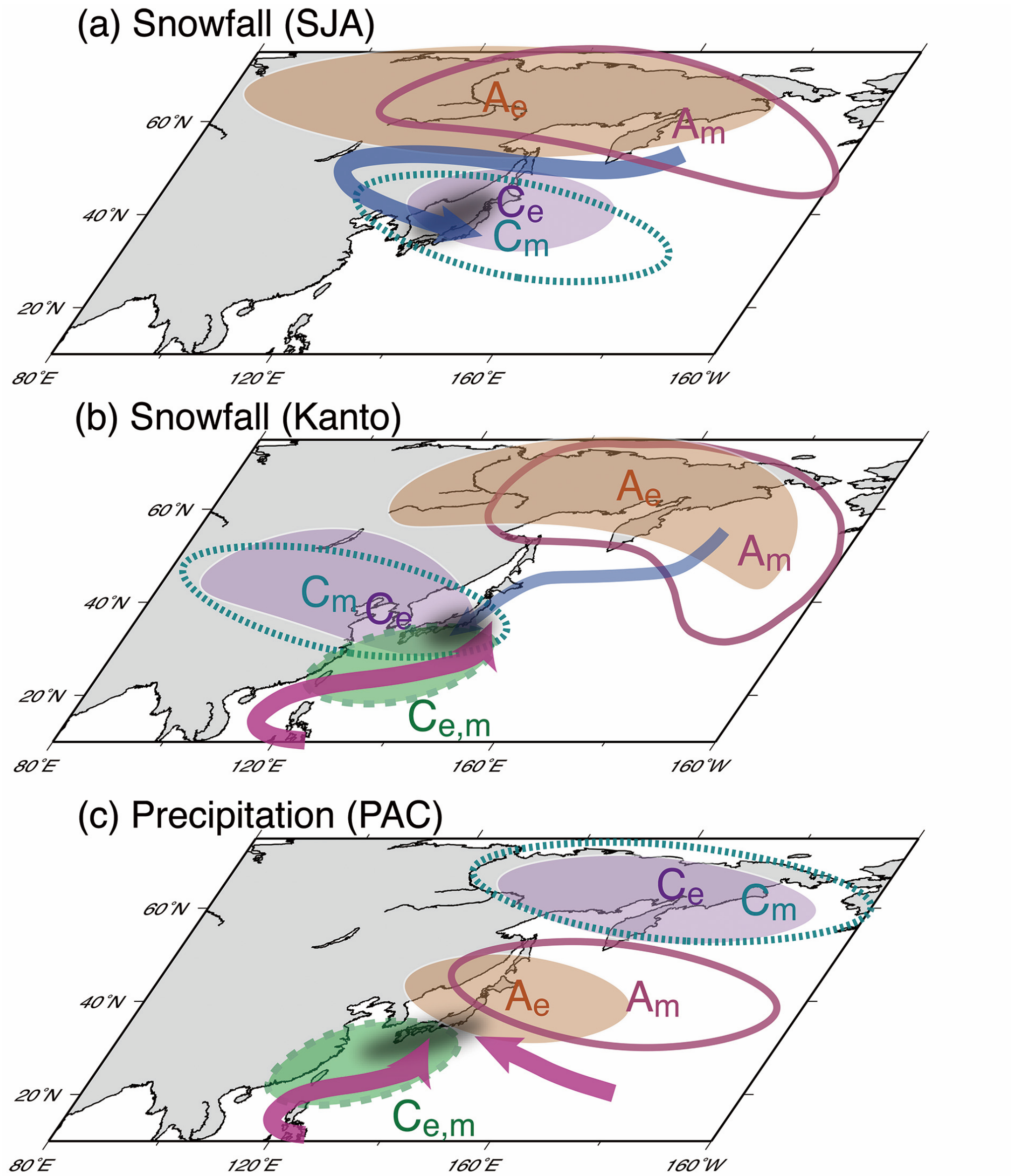
(a) Snowfall (SJA)
Ae
Am
Ce
Cm
60°N
40°N
20°N
80°E
120°E
160°E
160°W
(b) Snowfall (Kanto)
Ae
Am
Cm
Ce
Ce,m
(c) Precipitation (PAC)
Ce
Cm
Ae
Am
Ce,m